



# TIC 278956474: Two Close Binaries in One Young Quadruple System Identified by TESS

Pamela Rowden<sup>1</sup> , Tamás Borkovits<sup>2,3</sup> , Jon M. Jenkins<sup>4</sup> , Keivan G. Stassun<sup>5,6</sup> , Joseph D. Twicken<sup>4,7</sup> , Elisabeth R. Newton<sup>8</sup> , Carl Ziegler<sup>9</sup> , Coel Hellier<sup>10</sup> , Aylin Garcia Soto<sup>8</sup> , Elisabeth C. Matthews<sup>11</sup> , Ulrich Kolb<sup>1</sup> , George R. Ricker<sup>11</sup> , Roland Vanderspek<sup>11</sup> , David W. Latham<sup>12</sup> , S. Seager<sup>11,13,14</sup> , Joshua N. Winn<sup>15</sup> , Luke G. Bouma<sup>15</sup> , César Briceño<sup>16</sup> , David Charbonneau<sup>12</sup> , William Fong<sup>11</sup> , Ana Glidden<sup>11,13</sup> , Natalia M. Guerrero<sup>11</sup> , Nicholas Law<sup>17</sup> , Andrew W. Mann<sup>17</sup> , Mark E. Rose<sup>4</sup> , Joshua Schlieder<sup>18</sup> , Peter Tenenbaum<sup>4,7</sup> , and Eric B. Ting<sup>4</sup>

<sup>1</sup> School of Physical Sciences, The Open University, Milton Keynes MK7 6AA, UK; [pam.rowden27@gmail.com](mailto:pam.rowden27@gmail.com)

<sup>2</sup> Baja Astronomical Observatory of Szeged University, H-6500 Baja, Szegedi út, kt. 766, Hungary

<sup>3</sup> Konkoly Observatory, Research Centre for Astronomy and Earth Sciences, H-1121 Budapest, Konkoly Thege Miklós út 15-17, Hungary

<sup>4</sup> NASA Ames Research Center, Moffett Field, CA 94035, USA

<sup>5</sup> Department of Physics and Astronomy, Vanderbilt University, Nashville, TN 37235, USA

<sup>6</sup> Department of Physics, Fisk University, Nashville, TN 37208, USA

<sup>7</sup> SETI Institute, Mountain View, CA 94043, USA

<sup>8</sup> Department of Physics and Astronomy, Dartmouth College, Hanover, NH 03755, USA

<sup>9</sup> Dunlap Institute for Astronomy and Astrophysics, University of Toronto, 50 St. George Street, Toronto, Ontario M5S 3H4, Canada

<sup>10</sup> Astrophysics Group, Keele University, Staffordshire, ST5 5BG, UK

<sup>11</sup> Department of Physics and Kavli Institute for Astrophysics and Space Research, Massachusetts Institute of Technology, Cambridge, MA 02139, USA

<sup>12</sup> Center for Astrophysics | Harvard & Smithsonian, 60 Garden Street, Cambridge, MA 02138, USA

<sup>13</sup> Department of Earth, Atmospheric and Planetary Sciences, Massachusetts Institute of Technology, Cambridge, MA 02139, USA

<sup>14</sup> Department of Aeronautics and Astronautics, MIT, 77 Massachusetts Avenue, Cambridge, MA 02139, USA

<sup>15</sup> Department of Astrophysical Sciences, Princeton University, 4 Ivy Lane, Princeton, NJ 08544, USA

<sup>16</sup> Cerro Tololo Inter-American Observatory, Casilla 603, La Serena, Chile

<sup>17</sup> Department of Physics and Astronomy, The University of North Carolina at Chapel Hill, Chapel Hill, NC 27599-3255, USA

<sup>18</sup> NASA Goddard Space Flight Center, 8800 Greenbelt Rd, Greenbelt, MD 20771, USA

Received 2020 April 28; revised 2020 June 2; accepted 2020 June 10; published 2020 July 23

## Abstract

We have identified a quadruple system with two close eclipsing binaries in Transiting Exoplanet Survey Satellite (TESS) data. The object is unresolved in Gaia and appears as a single source at parallax  $1.08 \pm 0.01$  mas. Both binaries have observable primary and secondary eclipses and were monitored throughout TESS Cycle 1 (sectors 1–13), falling within the TESS Continuous Viewing Zone. In one eclipsing binary ( $P = 5.488$  days), the smaller star is completely occluded by the larger star during the secondary eclipse; in the other ( $P = 5.674$  days) both eclipses are grazing. Using these data, spectroscopy, speckle photometry, spectral energy distribution analysis, and evolutionary stellar tracks, we have constrained the masses and radii of the four stars in the two eclipsing binaries. The Li I equivalent width indicates an age of 10–50 Myr and, with an outer period of  $858_{-5}^{+7}$  days, our analysis indicates this is one of the most compact young 2 + 2 quadruple systems known.

*Unified Astronomy Thesaurus concepts:* Close binary stars (254); Eclipsing binary stars (444); Young stellar objects (1834); Multiple stars (1081)

## 1. Introduction

The main purpose of the Transiting Exoplanet Survey Satellite (TESS; Ricker et al. 2014), is to identify nearby planets  $\leq 4 R_{\oplus}$  that can be fully characterized. However, a great deal of complementary science has come from the mission, particularly in stellar science (see for example Fausnaugh et al. 2019; Holoiën et al. 2019; Huber et al. 2019; Schofield et al. 2019; Zhan et al. 2019; Ahlers et al. 2020).

Eclipsing binaries (EBs) are known to be detected in transiting exoplanet surveys. Around 16% of Kepler Objects of Interest (KOIs) have been identified by the Kepler pipeline as EBs, and a further  $\approx 7\%$  as background EBs.<sup>19</sup> Moreover, the Kepler and K2 missions have also identified triple and quadruple eclipsing systems and even a bound quintuple system (KOI 3156) exhibiting eclipses of at least three different subsystems (Helminiak et al. 2017).

Raghavan et al. (2010) estimate that, among solar-type stars,  $33\% \pm 2\%$  of systems are binary,  $8\% \pm 1\%$  of systems are triple, and  $3\% \pm 1\%$  are composed of four or more stars. As an all-sky survey, TESS can be expected to identify a proportion of these rarer multiple-star systems.

We use TESS data to identify a 2 + 2 quadruple star system (TIC 278956474) with two short-period inner binaries. We estimate the age of TIC 278956474 as 10–50 Myr (Section 2.6), making this a young system. Known young quadruple systems include GG Tauri (Guilloteau et al. 1999; Köhler 2011), HD 98800 (Tokovinin 1999; Ribas et al. 2018), HD 34700 (Sterzik et al. 2005), AB Doradus (Janson et al. 2007; Wolter et al. 2014), AO Vel (González et al. 2006, 2008a, 2008b), HD 91962 (Tokovinin et al. 2015), LkCa 3 (Torres et al. 2013; Baraffe et al. 2015), and HD 86588 (Tokovinin et al. 2018). IRS5 might be a young quadruple system (Chen et al. 2015). LkH $\alpha$  263C, around which a circumstellar disk has been identified (Jayawardhana et al. 2002), appears to be a member of a young quadruple system in the MBM 12 association.

<sup>19</sup> <https://exoplanetarchive.ipac.caltech.edu/>

While considering the binary population of young clusters, Marks & Kroupa (2012) demonstrated from simulations that clusters with a formal binary fraction of unity at birth will evolve to a lower binary fraction over time. They note that younger clusters appear to have a higher binary fraction than older clusters with a similar stellar density (see for example Duchêne & Kraus 2013). Thus, studying the population of young quadruple systems such as TIC 278956474 is of interest when considering the evolution of the binary fraction of stellar clusters over time.

This paper is organized as follows. In Section 2 we discuss the data. In Section 3 we present our models, which confirm that this is a young 2 + 2 quadruple system. The models are discussed in Section 4; in particular, we consider the dynamical properties of the system, as well as its place among known young quadruple star systems. Our conclusions are drawn in Section 5.

## 2. Data

Table 1 gives some basic data on TIC 278956474, such as alternative names, position, proper motion, and magnitudes in various passbands. The data are drawn from Exofop,<sup>20</sup> and from Gaia DR2.<sup>21</sup>

### 2.1. SPOC Data

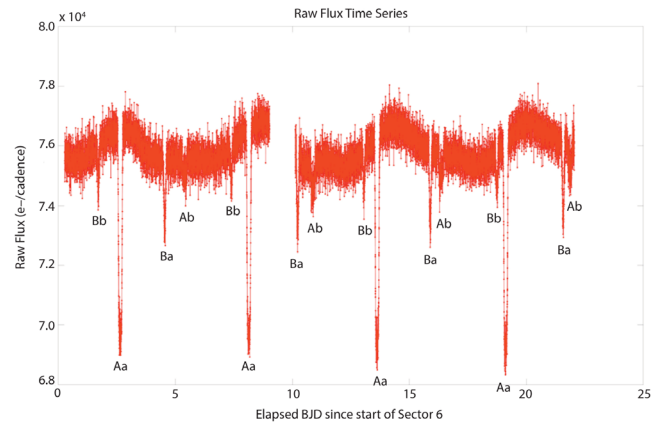
Threshold crossing events (TCEs) were identified in observations of TIC 278956474 in two minute cadence data, processed by NASA’s TESS Science Processing Operations Center (SPOC) (Jenkins et al. 2016; Jenkins 2019). TIC 278956474 lies in the Southern Continuous Viewing Zone near the southern ecliptic pole and was observed on camera 4 throughout TESS Cycle 1 (Sectors 1–13). We focus on the depth of each SPOC TCE in ppm.

Figure 1 illustrates the simple aperture photometry light curve (Twicken et al. 2010; Morris et al. 2017) for sector 6, annotated to highlight the eclipses. Similar information is available on all 13 sectors, and is included in the publicly available data validation reports hosted on MAST.

Selected data on this target from SPOC data validation reports (Twicken et al. 2018; Li et al. 2019) are presented in Table 2 (multi-sector analysis, sectors 1–13) and in Table A1 (all single-sector and multi-sector analyses).

The deepest eclipse and the shallowest eclipse both relate to the same binary (“A”). This binary has a period of 5.488 days. We label the two components Aa and Ab. The second binary (“B”) has a period of 5.674 days, and its components are labeled Ba and Bb.

The SPOC analysis indicates that both eclipses in B are V-shaped, while both eclipses in A are U-shaped. This indicates the eclipses in B are grazing, while in A star Ab is fully occluded as it passes behind Aa. We obtain a preliminary estimate of the ratio of the radii of Ab:Aa ( $\approx 0.29$ ) by comparing the ingress duration with the total eclipse duration. See Figure 2 for a cartoon illustrating the relative radii of the four stars to scale and the proportion of each star that is occluded during an eclipse. Each pair of stars is positioned as it would be at the middle of the primary transit, given the approximate angle of inclination, as observed by TESS.



**Figure 1.** Simple aperture photometry light curve for Sector 6, annotated to indicate the various eclipses. The start Barycentric Julian Date (BJD) for Sector 6 is 2458468.

**Table 1**  
Basic Data on TIC 278956474

Parameter	Value
Alternative names <sup>a</sup>	UCAC4 165-008872 2MASS J06454123-5708171 WISE J064541.25-570817.0 APASS 27316174
R.A. <sup>a,b</sup>	101°421895
Decl. <sup>a,b</sup>	−57°138098
$l^a$	266°7396
$b^a$	−23°2743
Parallax <sup>b</sup>	1.08 ± 0.01 mas
Proper motion R.A. <sup>b</sup>	4.29 ± 0.03 mas yr <sup>−1</sup>
Proper motion decl. <sup>b</sup>	−2.21 ± 0.03 mas yr <sup>−1</sup>
$B^a$	14.191 ± 0.052
Gaia bp <sup>b</sup>	13.7641
$V^a$	13.542 ± 0.092
Gaia <sup>a,b</sup>	13.4153 ± 0.000408
TESS <sup>a</sup>	12.9637 ± 0.006
Gaia rp <sup>b</sup>	12.9020
$J^a$	12.291 ± 0.022
$H^a$	11.951 ± 0.024
$K^a$	11.835 ± 0.021
WISE 3.4 $\mu\text{m}^a$	11.813 ± 0.023
WISE 4.6 $\mu\text{m}^a$	11.826 ± 0.021
WISE 12 $\mu\text{m}^a$	12.048 ± 0.178
WISE 22 $\mu\text{m}^a$	9.681

**Notes.** Sources.

<sup>a</sup> Exofop <https://exofop.ipac.caltech.edu/tess/>.

<sup>b</sup> Gaia DR2 <https://gea.esac.esa.int/archive/>.

### 2.2. WASP-South Photometry

WASP-South was the southern station of the WASP transit-search project (Pollacco et al. 2006), situated in Sutherland, South Africa. It observed the field of TIC 278956474 for four consecutive years from 2008 September, spanning 170 nights each year, and obtaining a total of 26,700 photometric data points. The observations used 200 mm,  $f/1.8$  lenses with a 400–700 nm passband, backed by 2048 × 2048 CCDs. Reduction with the WASP pipeline produced photometry

<sup>20</sup> <https://exofop.ipac.caltech.edu/tess/>

<sup>21</sup> <https://gea.esac.esa.int/archive/>

**Table 2**  
Data from SPOC

Component	Sector	Period (days)	Depth (ppm)	Duration (hr)	Ingress (hr)	Odd depth (ppm)	Even depth (ppm)	Secondary depth (ppm)
Aa	1–13	$5.488035 \pm 0.000005$	$93900 \pm 200$	$5.43 \pm 0.01$	$1.22 \pm 0.01$	$94600 \pm 300$	$93300 \pm 300$	$8900 \pm 400$
Aa	1–13*	$5.488036 \pm 0.000005$	$93900 \pm 200$	$5.43 \pm 0.01$	$1.22 \pm 0.01$	$94500 \pm 300$	$93400 \pm 300$	Component Ab
Ab	1–13	$2.74403 \pm 0.00002$	$8900 \pm 200$	$5.29 \pm 0.09$	$1.0 \pm 0.1$	Model fitter failed	Model fitter failed	n/a
Ab	1–13*	$5.48808 \pm 0.00004$	$8900 \pm 200$	$5.29 \pm 0.08$	$1.0 \pm 0.1$	$9000 \pm 300$	$8700 \pm 300$	Component Aa
B	1–13	$2.837163 \pm 0.000007$	$25100 \pm 200$	$3.34 \pm 0.03$	$1.67 \pm 0.02$	$16400 \pm 300$	$33400 \pm 300$	n/a
B	1–13*	$2.837162 \pm 0.000007$	$25100 \pm 200$	$3.34 \pm 0.03$	$1.67 \pm 0.02$	$16400 \pm 200$	$33400 \pm 300$	n/a

**Note.** The secondary in component Aa coincides with the time of the primary in component Ab, and vice versa. Similarly for components Ba and Bb. Secondary depths are therefore only included where each component is not separately identified, as is the case with B in this table, which has been identified at half the true period. A second science run was completed for multi-sector 1–13 in order to identify component Ab at the correct period and to remove the partial eclipse of Aa at the end of sector 8. This science run is identified as sector 1–13\*. For data from each sector, see Table A1.

relative to other stars in the field with an extraction aperture of  $48''$ . At a Gaia magnitude of 13.4, the star is at the faint end of the WASP range, but the data are sufficient to detect 10% eclipses.

### 2.3. Period Study

One way to determine whether two EBs producing a blended lightcurve are physically bound is to find anti-correlated eclipse timing variations (ETV) in the two pairs. Similar anti-correlated ETVs have proven the real, bound  $2 + 2$  quadruple nature of V994 Her (Lee et al. 2008; Zasche & Uhlař 2016) and EPIC 220204960 (Rappaport et al. 2017). More recently, Zasche et al. (2019) performed a thorough analysis of a larger sample of doubly EBs found within the frame of the several year-long photometry of the Optical Gravitational Lensing Experiment survey (Udalski et al. 2015), and identified 28 systems where the ETVs showed evidence of the light-travel time effect (LTTE) caused by the relative motion of the two binaries around their common center of mass and/or perturbations due to the dynamical interactions of the two binaries. To search for ETVs in the two EBs in TIC 278956474, we determined the times of minimum light of each eclipse observed with TESS in the same manner as was described in Section 5 of Borkovits et al. (2018).

In summary, after removing the eclipses of the other binary the light curves were phase folded, binned into 1000 equally phased cells, and averaged within each cell. In this way we obtained disentangled, phase-folded light curves for both binaries (see Figure 3). Then, the eclipses of these light curves were fitted with 8–10th-order polynomials, and in this way we obtained separate templates for both the primary and secondary eclipses. These templates were then fitted to each individual eclipse events. (Naturally, we excluded those events that were affected by any eclipses of the other binary.) We obtained  $\sim 4 \times 50$  separate minima times (primary and secondary eclipses for both systems) (Tables B1 and B2). In what follows, however, we concentrate only on the ETVs of the two primary eclipses, as the secondary ETV points, determined from shallower eclipses, have much higher scatter.

We also took into account the historical WASP-South observations (see Section 2.2). These data have large scatter, and therefore are unsuitable for determining individual eclipse

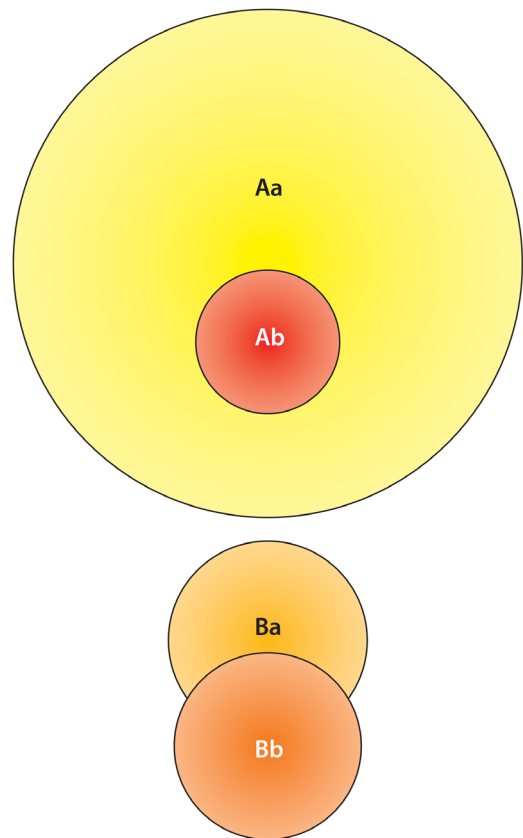


**Figure 2.** Cartoon showing the relative sizes of the four stars to scale and the proportions of the stars that are occluded during eclipses. Each pair of stars is positioned as it would be at the middle of the primary transit, given the approximate angle of inclination, as observed by TESS.

times. However, folding these measurements with the period of binary A season by season, we were able to determine additional seasonal primary minimum times for binary A with a reasonable accuracy. These four seasonal minima are also tabulated in Tables B1 and B2.

We plot the ETVs of the primary eclipses of both binaries in the two panels of Figure 4. The anti-correlated nature of the nonlinear timing variations of both binaries is clearly visible. The most likely origin of this feature is the LTTE, which arises

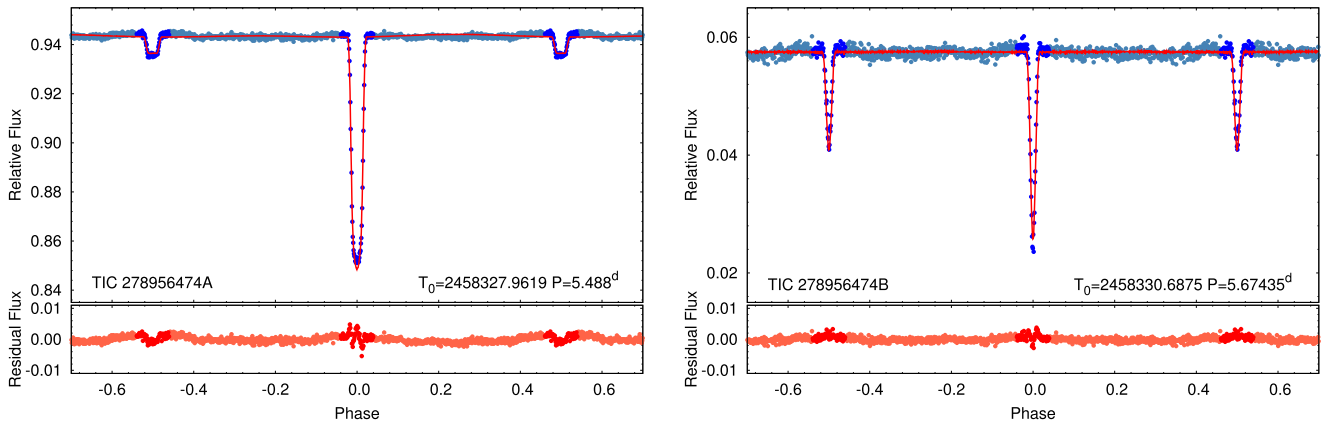


**Figure 3.** Disentangled, phase-folded, binned, averaged light curves (blue points) of binaries A (left) and B (right), together with the complex model solution light curves (see Section 3.2), processed in the same manner. (For the joint analysis only the darker blue points were used.) The lowest, residual data were also obtained with phase-folding, binning, and averaging the residual curve of the complete light-curve model.

from the varying distances of the two binaries from the Earth during their revolution around the common center of mass of the whole quadruple system. Therefore, the ETVs strongly suggest that TIC 278956474 is one of the tightest known physically bound  $2 + 2$  quadruple systems. This question will be discussed further in Section 3.2.

#### 2.4. Gaia DR2

TIC 278956474 was identified by Gaia (Gaia Collaboration et al. 2016, 2018; Andrae et al. 2018; Riello et al. 2018) as a single source with a mean Gaia magnitude of 13.4 and a parallax of  $1.08 \pm 0.01$  mas, corresponding to a distance of  $926 \pm 12$  pc. Various systematic corrections to Gaia parallaxes have been proposed. The online documentation for Gaia DR2 states a correction of  $-0.03$  mas may be appropriate. The probabilistically derived distance in Bailer-Jones et al. (2018) indicates a distance of  $903_{-9}^{+12}$  pc for TIC 278956474, which corresponds to an offset of  $-0.03$  mas. Schönrich et al. (2019) find that on average the parallax offset is  $-0.054$  mas, while Stassun & Torres (2018) find evidence for a systematic offset of  $-0.082 \pm 0.033$  mas, for brightnesses  $G \geq 12$  and for distances 0.03–3 kpc. All agree that Gaia parallaxes as recorded in the data releases are too small. Despite this, our best-fit model (Section 3.2) indicates that the uncorrected Gaia parallax for this system is slightly too large and that the true distance is  $958 \pm 23$  pc.

Gaia DR2 assigns a renormalized unit weight error (RUWE) to each source, where a value of 1.0 indicates the source is likely to be a single star, and a value  $\geq 1.4$  indicates that the source is likely to be non-single or otherwise problematic for the astrometric solution, for example a  $\leq 1''$  binary. The RUWE for TIC 278956474 is 1.06. However, we know from the TESS data that TIC 278956474 is a  $2 + 2$  quadruple system, not a single star. The low Gaia DR2 RUWE value suggests the two binaries are likely to be tightly bound.

Gaia DR2 does not specify an extinction for this system. We use several sources to estimate extinction in the Gaia passband. From the catalog of Lallement et al. (2019), which uses Gaia and Two Micron All Sky Survey (2MASS) photometric data to estimate the extinction toward 27 million carefully selected target stars with a Gaia DR2 parallax uncertainty below 20%, we estimate the extinction at 0.196 in the Gaia passband, although it should be noted that the region in question falls

outside the edges of the dust map and hence the reddening is estimated.

Dust maps from Schlegel et al. (1998) indicate the extinction in the V band along the line of sight is  $0.198 \leq A_V \leq 0.224$  (mean  $0.212 \pm 0.007$ ), and dust maps from Schlafly & Finkbeiner (2011) indicate the extinction along the line of sight is  $0.170 \leq A_V \leq 0.193$  (mean  $0.182 \pm 0.002$ ).

An online tool<sup>22</sup> estimating  $N_{\text{HI}}$  and  $N_{\text{H}_2}$  from 493 afterglows detected by the Swift X-Ray Telescope (Willingale et al. 2013) returns  $N_{\text{H,tot}} 7.76 \times 10^{20}$  atoms  $\text{cm}^{-2}$  (mean),  $7.34 \times 10^{20}$  atoms  $\text{cm}^{-2}$  (weighted). Using the relation between  $N_{\text{H}}$  and  $A_V$  in Güver & Özel (2009),  $A_V$  is  $0.35 \pm 0.01$  (mean),  $0.33 \pm 0.01$  (weighted).

This is higher than other estimates, but is in line with the findings in our model of  $E(B - V) = 0.108_{-0.012}^{+0.025}$  mag (Section 3.2).

#### 2.5. Speckle Photometry

If the pair of binaries is widely separated, high angular resolution imaging may be able to resolve the system or detect additional nearby stars. We searched for stellar companions to TIC 278956474 with speckle imaging on the 4.1 m Southern Astrophysical Research telescope (Tokovinin 2018) on 2020 January 7 UT, observing in a similar visible bandpass as TESS. More details of the observations are available in Ziegler et al. (2020). The  $5\sigma$  detection sensitivity and speckle auto-correlation functions from the observations are shown in Figure 5. The seeing during the night was below average, resulting in a shallow detection curve, and the binaries, assuming a  $\Delta_m = 2$  in the TESS bandpass, would likely be resolved at angular separations greater than approximately  $0''.12$ , corresponding to a projected separation of  $\sim 115$  au at the estimated distance to the system, based on the uncorrected stellar parallax. No nearby stars, however, were detected within  $3''$  of TIC 278956474, placing an upper limit for projected separations of the binaries at approximately 115 au.

Points that appear a little less than  $1''$  east, west, north, and south of the target are artefacts of the data.

The TESS Input Catalog identifies a 19th-magnitude star  $11''.48$  from the target,  $106^\circ.63$  E of N, and a 17th-magnitude star  $15''.77$  from the target,  $141^\circ.72$  E of N. Both these stars

<sup>22</sup> <https://www.swift.ac.uk/analysis/nhtot/index.php>

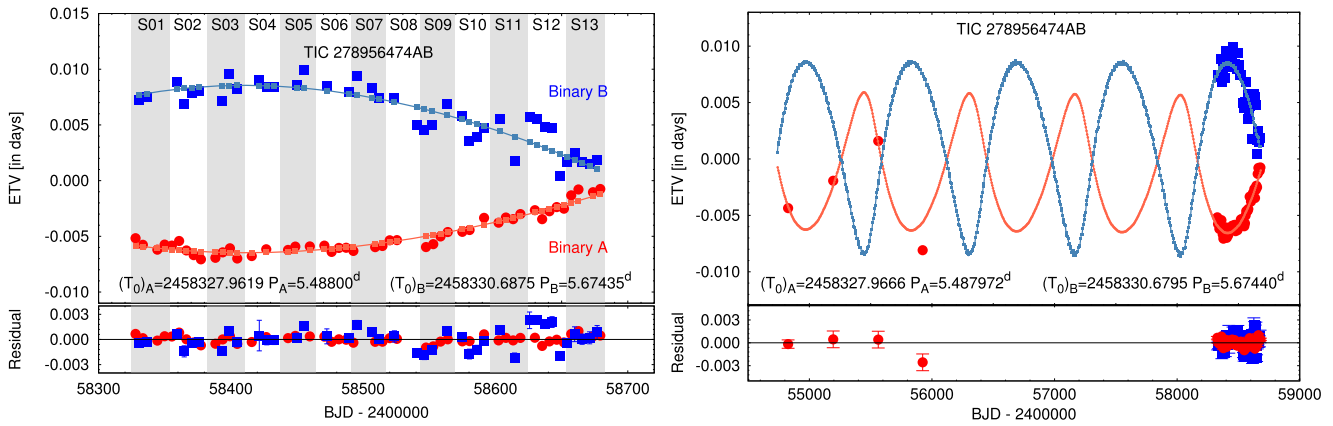


**Figure 4.** Eclipse timing variations (ETVs) of the primary minima of TIC 278956474A and B (red and blue, respectively). The anti-correlated nature of the nonlinear timing variations, most likely due to the light-travel time effect, occurs due to the revolution of the barycentres of the two binaries around the common center of mass of the quadruple. Lighter red and blue lines represent the model solutions obtained through the combined light-, ETV-, and radial velocity-curve analysis, discussed in Section 3.2. The left panel displays the ETVs during the first year of TESS observations, while the four earlier primary minima of binary A derived from the seasonal average light curves of the historical WASP-South observations are also plotted in the right panel.

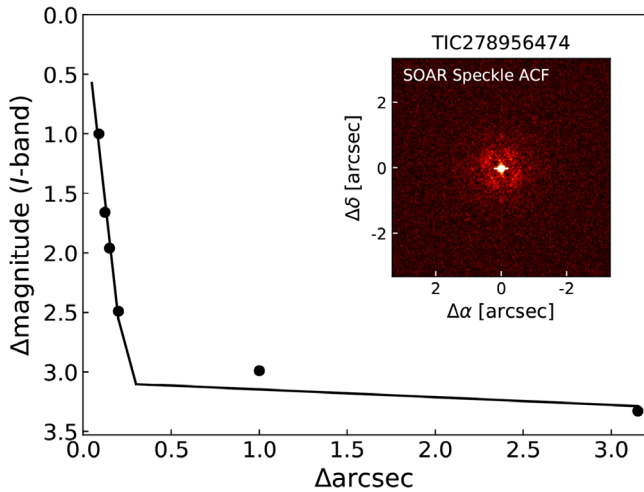


**Figure 5.** Speckle imaging auto-correlation function (inset) and resulting contrast curve obtained on 2020 January 7 with speckle imaging on the 4.1 m Southern Astrophysical Research telescope. This observation places an upper limit for the projected separation of the binaries at approximately 115 au.

were also observed by Gaia, and Gaia does not identify any other stars that are closer. From the difference images in the SPOC data validation reports, it is highly unlikely that the eclipses analyzed here arise from these known near neighbors.

## 2.6. Spectroscopy

We obtained two spectra using the High Resolution Spectrograph (Crause et al. 2014) on the South African Extremely Large Telescope (Buckley et al. 2006). We obtained spectra on the nights of 2019 October 3 and 4. The spectra were reduced using the MIDAS pipeline (Kniazev et al. 2016, 2017).<sup>23</sup> The wavelength calibration used ThAr and Ar lamps. The resulting resolution was about 46,000 and the spectra spanned 370–980 nm.

Separating the components in the spectra is challenging. The second-brightest component (Ba) contributes only a few percent of the total light in the optical and any attempt to

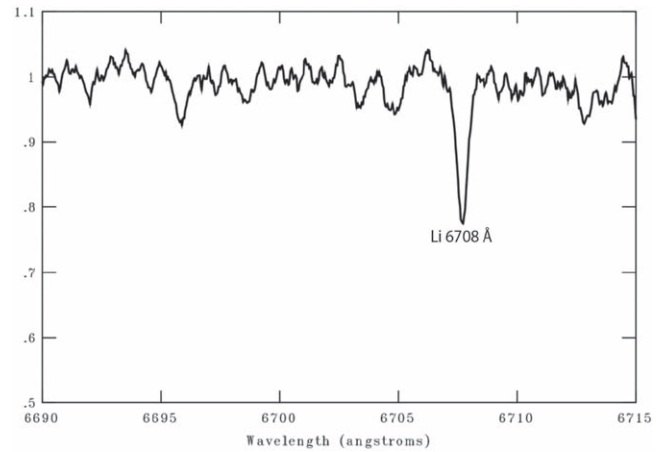


**Figure 6.** Spectra obtained on the High Resolution Spectrograph on the South African Extremely Large Telescope indicate a Li 6708 Å equivalent width of  $143 \pm 10$  mÅ for the whole system.

disentangle the Aa and Ba would be complicated by the presence of the two fainter components, Ab and Bb. We do note absorption of H $\alpha$  and H $\beta$ , as well as Ca II at  $\approx 8664$  and  $8545$  Å. These features are consistent with our model of the brightest star (Section 3.2).

We also identified a clear and strong Li absorption feature at 6708 Å (Figure 6). The average equivalent width (EW) is  $143 \pm 10$  mÅ. This is almost entirely due to star Aa: the next most significant star, Ba, contributes  $\approx 3\%$  of the light.

By comparison with Figure 4 of Aarnio et al. (2008), this EW in a star of the  $T_{\text{eff}}$  of Aa (6180 K: Section 3.2) is consistent with an age of 30–50 Myr and, by comparison with Figure 5 of Mentuch et al. (2008), with stars in the  $\beta$  Pictoris moving group ( $21 \pm 9$  Myr, Mentuch et al. 2008;  $22 \pm 6$  Myr, Shkolnik et al. 2017;  $24 \pm 3$  Myr, Bell et al. 2015) and the Tucanae–Horologium association (isochronal age 20–30 Myr, Kraus et al. 2014;  $28 \pm 11$  Myr, Mentuch et al. 2008; Li depletion age  $\approx 40$  Myr, Kraus et al. 2014;  $45 \pm 4$  Myr, Bell et al. 2015).

Estimating  $V - K$  for star Aa using the  $T_{\text{eff}}$ , distance, and extinction from our model (Section 3.2), we referred to Riedel et al. (2017), who considered the Li depletion (Figure 21) and ages (Table 1 and references therein) of stars in nearby young

<sup>23</sup> [http://www.sao.ac.za/~akniazev/pub/HRS\\_MIDAS/HRS\\_pipeline.pdf](http://www.sao.ac.za/~akniazev/pub/HRS_MIDAS/HRS_pipeline.pdf)

moving groups (NYMGs). This indicates that TIC 278956474 is likely to be younger than AB Doradus (50–150 Myr), Carina-Near (150–250 Myr), and Ursa Major (300–500 Myr); older than  $\epsilon$  Chamaeleontis (5–8 Myr),  $\eta$  Chamaeleontis (6–11 Myr), and TW Hydrae (3–15 Myr); and consistent with stars in the following NYMG:  $\beta$  Pictoris (10–24 Myr), Octans (20–40 Myr), Tucana-Horologium (30–45 Myr), and Argus (35–50 Myr).

From the Li I EW, we therefore estimate the age of the system to be 10–50 Myr.

In Figure 6 the Li 6708 Å feature has been Doppler shifted to its rest wavelength. Relative to the rest wavelength, the heliocentric radial velocities (RVs) are  $75.2 \pm 1.8 \text{ km s}^{-1}$  on the first night and  $36.7 \pm 2.2 \text{ km s}^{-1}$  on the second night.

### 3. Models

#### 3.1. Preliminary Estimates

We made preliminary estimates of the properties of the stars in the system as follows.

Component Ab is fully occluded when it passes behind Aa. Gaia obtained 191 astrometric observations of the system, of which 189 were considered good and two bad. Considering that both binaries would have been out of transit for about 86% of the observing time, and that the difference between the TESS magnitude  $T$  and the Gaia magnitude in the red passband  $G_{BP}$  is only 0.06 mag and that generally  $T \approx G_{BP}$ , it is likely that the magnitude of the system in the  $G$  passband (300–1100 nm) reflects the out-of-transit magnitude of the system. The luminosity of Ab in the Gaia passband can therefore be estimated from the total luminosity of the system, taking into account the Gaia magnitude, the Gaia parallax, and an appropriate estimate of extinction (Section 2.4). The luminosity of Ab was estimated as  $0.0247_{-0.005}^{+0.006} L_{\odot}$  using the correction from Stassun & Torres (2018) and  $0.0279_{-0.007}^{+0.008} L_{\odot}$  using the uncorrected Gaia parallax, in both cases using  $A_G$  from Lallment et al. (2019).

We used a library of single-star evolutionary models from the Binary Stellar Evolution Population Synthesis (BiSEPS) code (Willems & Kolb 2002, 2004; Willems et al. 2006; Davis et al. 2010; Farmer et al. 2013) to approximate the likely radius, mass, effective temperature, and age of Ab, assuming solar metallicity. This allowed us to eliminate the possibility that Ab was a white dwarf.

Comparing the ingress with the total eclipse time during the primary eclipse of A indicated that the ratio of the radii of the two stars was likely to be of the order of 0.29, which indicated that Aa was not evolved and was further confirmation that neither star was a white dwarf. From this and the relationship between the luminosity of Aa and Ab in the TESS passband (600–1000 nm centered on 786.5 nm), we estimated the radius and bolometric luminosity of Aa, also at solar metallicity.

We then used stellar evolution tracks from Modules for Experiments in Stellar Astrophysics (MESA) (Paxton et al. 2011, 2013, 2015) to refine our parameters for Aa and Ab, again assuming solar metallicity. From this we estimated the initial mass and  $T_{\text{eff}}$  of Aa as  $1.315 M_{\odot}$  and 6456 K respectively: these estimates would be used as the starting point for the more in-depth analysis described in Section 3.2, which makes use of the PAdova and TRieste Stellar Evolution Code (PARSEC) (Bressan et al. 2012) stellar evolutionary tracks.

BiSEPS evolves both single stars and binary systems self-consistently from formation to compact remnant. While not a full stellar evolutionary code, the library of models this code produces was useful in obtaining “ballpark” figures for later investigation. MESA and PARSEC, by contrast, are both full stellar evolutionary codes, evolving stars from pre-main sequence (PMS) to compact remnant. MESA provides information on what is happening in the core as well as on the surface.

#### 3.2. Combined Light-, RV-, and ETV-curve Analysis with and without Joint SED and PARSEC Evolutionary Track Modeling

We carried out combined, simultaneous analysis of the full TESS Cycle 1 light-curve data together with the ETV data calculated from both TESS and WASP-South light curves for the primary eclipses of both binaries (Section 2.3), and also of the two RV data points derived from the spectroscopic observations (Section 2.6). Several advantages of such a simultaneous analysis are discussed, e.g., in Borkovits et al. (2018).

For the analysis we prepared the data sets as follows. We downloaded the calibrated two-minute data files for each sector from the MAST portal.<sup>24</sup> For the double-binary model analysis we detrended the lightcurve with the software package WÖTAN (Hippke et al. 2019). In this way we removed not only any instrumental effects, but also those light-curve variations that might have arisen from the rotation and probable chromospheric activities of the targets, but are not relevant for the binary star modeling. Then, to save substantial computational time we binned the two-minute cadence data, averaging them every half hour (1800 s). Finally, we kept only those light-curve points that were within the  $\pm 0.04$  phase-domain regions around each eclipse. These segments of the light curve were modeled simultaneously with the two ETV curves of the primary eclipses of both binaries (see Section 2.3). Note that some outliers were omitted from the analyzed ETV curves. These points are denoted with an asterisk in Tables B1 and B2.

Finally, we included in the analysis the two RV points (BJD = 2,458,760.5678;  $\text{RV} = +75.2 \pm 1.8 \text{ km s}^{-1}$ , and 2,458,761.5605;  $+36.7 \pm 2.2 \text{ km s}^{-1}$ ).

For our analysis we used the software package LIGHT-CURVEFACTORY (Borkovits et al. 2018, 2019b). This package is able to model the light, ETV, and RV curves of any configurations of eclipsing systems formed by 2–4 stars (i.e., binary, triple, and quadruple star systems). To solve the inverse problem, the software employs a Markov chain Monte Carlo parameter search based on an implementation of the generic Metropolis–Hastings algorithm (see, e.g., Ford 2005).

In the first stage of the analysis the temperature ( $T_{Aa}$ ) and the mass of the primary ( $m_{Aa}$ ) of binary A were kept fixed on the values given in Section 3.1, while the 21 adjusted parameters were as follows.

- (i) Seven light curve-related parameters: temperature ratios ( $T_b/T_a$ )<sub>A,B</sub> and  $T_{Ba}/T_{Aa}$ ; the durations of the two primary eclipses ( $\Delta t_{\text{pri}}$ )<sub>A,B</sub> (which are closely related to the sum of the fractional radii of the binary stars; see Rappaport et al. 2017 for an explanation); and the ratios of the radii in both binaries ( $R_b/R_a$ )<sub>A,B</sub>.

<sup>24</sup> <https://mast.stsci.edu/portal/Mashup/Clients/Mast/Portal.html>

**Table 3**

Median Values of the Parameters from the Double Eclipsing Binary Simultaneous Lightcurve, Single-lined Spectroscopic Binary Radial Velocity, Double ETV, and Joint SED and PARSEC Evolutionary Tracks Solution

Parameter	Binary A		Binary B		Outer orbit
$P$ (days)	5.488068 $^{+0.000016}_{-0.000010}$		5.674256 $^{+0.000017}_{-0.000030}$		858 $^{+7}_{-5}$
Semimajor axis ( $R_{\odot}$ )	15.70 $^{+0.09}_{-0.17}$		14.19 $^{+0.11}_{-0.10}$		543 $^{+5}_{-6}$
$i$ (deg)	88.97 $^{+0.16}_{-0.19}$		89.23 $^{+0.16}_{-0.08}$		85 $^{+3}_{-2}$
$e$	0		0		0.36 $^{+0.02}_{-0.03}$
$\omega$ (deg)	...		...		299 $^{+2}_{-2}$
$t_{\text{prim eclipse}}$ (BJD)	2 458 327.9619 $^{+0.0002}_{-0.0001}$		2 458 330.6870 $^{+0.0001}_{-0.0002}$		2 458 930 $^{+5a}_{-5}$
$\gamma$ (km s $^{-1}$ )	...		...		29 $^{+5}_{-3}$
Individual stars	Aa	Ab	Ba	Bb	
Relative quantities:					
Mass ratio ( $q = m_2/m_1$ )	0.357 $^{+0.009}_{-0.015}$		0.876 $^{+0.025}_{-0.049}$		0.691 $^{+0.016}_{-0.016}$
Fractional radius <sup>b</sup> ( $R/a$ )	0.1045 $^{+0.0018}_{-0.0020}$	0.0306 $^{+0.0005}_{-0.0006}$	0.0477 $^{+0.0019}_{-0.0023}$	0.0435 $^{+0.0015}_{-0.0014}$	
Fractional luminosity	0.927	0.010	0.043	0.020	
Physical quantities:					
$T_{\text{eff}}^c$ (K)	6180 $^{+99}_{-52}$	3680 $^{+84}_{-95}$	4472 $^{+126}_{-137}$	3876 $^{+131}_{-155}$	
Mass ( $M_{\odot}$ )	1.271 $^{+0.035}_{-0.046}$	0.451 $^{+0.016}_{-0.020}$	0.634 $^{+0.022}_{-0.017}$	0.550 $^{+0.020}_{-0.023}$	
Radius <sup>c</sup> ( $R_{\odot}$ )	1.641 $^{+0.036}_{-0.046}$	0.480 $^{+0.011}_{-0.014}$	0.674 $^{+0.026}_{-0.031}$	0.617 $^{+0.025}_{-0.024}$	
Luminosity <sup>c</sup> ( $L_{\odot}$ )	3.54 $^{+0.20}_{-0.18}$	0.038 $^{+0.004}_{-0.003}$	0.16 $^{+0.01}_{-0.01}$	0.079 $^{+0.011}_{-0.012}$	
( $M_{\text{bol}}$ )	3.40 $^{+0.06}_{-0.06}$	8.32 $^{+0.10}_{-0.10}$	6.74 $^{+0.10}_{-0.08}$	7.53 $^{+0.18}_{-0.15}$	
$\log g^c$ (cgs)	4.11 $^{+0.01}_{-0.01}$	4.73 $^{+0.02}_{-0.02}$	4.58 $^{+0.04}_{-0.03}$	4.60 $^{+0.03}_{-0.03}$	
$\log(\text{age})$ (dex)	7.00 $^{+0.03}_{-0.05}$	7.90 $^{+0.07}_{-0.07}$		7.70 $^{+0.05}_{-0.11}$	
[M/H](dex)		-0.37 $^{+0.10}_{-0.16}$			
$E(B - V)$ (mag)		0.108 $^{+0.025}_{-0.012}$			
( $M_V$ ) <sub>tot</sub> <sup>c</sup>		3.39 $^{+0.06}_{-0.06}$			
Distance (pc)		958 $^{+23}_{-23}$			

**Notes.**  $\gamma$  is the systemic radial velocity of the quadruple.<sup>a</sup> Time of periastron passage ( $\tau_{\text{out}}$ ).<sup>b</sup> Polar radii.<sup>c</sup> Interpolated from the PARSEC isochrones.

- (ii) Three orbital parameters for each binary: we allowed non-zero eccentricities for both binaries and, therefore,  $(e \cos \omega)_{A,B}$  and  $(e \sin \omega)_{A,B}$  were freely adjusted. The inclinations of the two orbits ( $i_{A,B}$ ) were also adjusted. However, the first sets of runs resulted in insignificantly low inner eccentricities ( $e_{A,B} \lesssim 10^{-3}$ ), so for later runs we assumed circular inner orbits and, therefore, inner eccentricities and arguments of periastrons were no longer adjusted.
- (iii) Five orbital parameters of the outer orbit: period ( $P_{\text{out}}$ ), time of periastron passage  $\tau_{\text{out}}$ , eccentricity, and argument of periastron as  $(e \cos \omega)_{\text{out}}$ ,  $(e \sin \omega)_{\text{out}}$  and, finally, the inclination  $i_{\text{out}}$ .
- (iv) Three mass parameters: the mass ratios of the two binaries ( $q_{A,B}$ ) and the mass of the primary of binary B ( $m_{Ba}$ ).

The two periods ( $P_{A,B}$ ) and reference primary eclipse times ( $(T_0)_{A,B}$ ) of both binaries were not adjusted, but constrained through the ETV curves, as was explained in Appendix A of Borkovits et al. (2019a). Furthermore, the systemic radial velocity of the center of mass of the whole quadruple system ( $\gamma$ ), which in the current model occurs only as an additive

parameter independent of any other parameters, was calculated in each trial step by simply minimizing a posteriori the goodness of fit of the RV curve (i.e.,  $\chi_{\text{RV}}^2$ ).

A logarithmic limb-darkening law was applied, interpolating the coefficients at each trial step with the use of the pre-computed passband-dependent tables of the PHOEBE software (Prša & Zwitter 2005).

Computing the orbital motion, and therefore the sky-projected positions of the four bodies, we assumed purely Keplerian orbits. Though the code has an in-built numerical integrator, and therefore numerical integration of the four-body motion, i.e., application of a photodynamical approach could be done easily, we found it unnecessary for the large  $P_{\text{out}}/P_{A,B}$  ratios which render the four-body perturbations undetectable, at least within the time domain of the available observations.

As a result of this combined analysis we obtained well constrained relative (i.e., dimensionless) stellar parameters (i.e., fractional radii and ratios of temperatures and masses). In order to obtain physical quantities within the frame of a self-consistent model, we added into the analysis the observed cumulative spectral energy distribution (SED) of the quadruple, and attempted to find consistent, co-eval PARSEC evolutionary tracks (Bressan et al. 2012) for all four stars. We generated

machine-readable PARSEC isochrone tables via the web based tool CMD 3.3.<sup>25</sup> These tables contain theoretically computed fundamental stellar parameters and absolute passband magnitudes in several different photometric systems, for a large three-dimensional grid of ages, metallicities, and initial stellar masses.

At this final stage of the simultaneous light curve, ETV curve, RV curve, SED, and evolutionary track modeling the adjusted parameters had slightly departed from those listed above. First, new adjustable quantities were also introduced, as three independent ages of stars Aa, Ab, and binary B<sup>26</sup> ( $\log \tau_{Aa, Ab, A}$ ), the metallicity [M/H] of the quadruple, the extinction parameter ( $E(B - V)$ ), and the distance ( $d$ ) of the system. Furthermore, the mass of the most prominent star Aa was no longer fixed, but allowed to adjust with the use of a simple uniform prior. In this way, the actual stellar masses, together with the given stellar ages and metallicity, determined the position of each star on the PARSEC tracks. Then, using a trilinear interpolation with the use of the closest grid points of the precalculated tables, the code interpolated the radii and temperatures of each star on one hand, and also their absolute passband magnitudes, for the SED fitting, on the other hand. These stellar radii and temperatures were used for the light-curve modeling (i.e., in contrast to the first stage, these quantities were no longer adjusted, but constrained instead). Furthermore, the interpolated absolute passband magnitudes transformed into model-observed passband magnitudes with the use of the extinction parameter and the system’s distance, and then their sum was compared to the observed magnitudes in each passband. In these final steps, distance ( $d$ ) was not a free parameter, but was constrained a posteriori in each trial step by minimizing the value of ( $\chi^2_{SED}$ ).

A more detailed description of this joint modeling process, including SED fitting with the use of PARSEC isochrone tables, can be found in Section 3 of Borkovits et al. (2020).

The results of this comprehensive analysis are tabulated in Table 3 and the model curves are plotted against the observed ETV and light curves in Figures 4 and 7. Moreover, for a better visualization of the model light curves of both binaries, we also plot the disentangled, phase-folded, binned, averaged versions of the solution light curve against the similarly processed detrended TESS light curves of the binaries in Figure 3. We tabulate the median values of each parameters together with the  $1\sigma$  uncertainties. These results will be discussed and compared with an independent SED analysis (Section 3.3) and MESA evolutionary tracks in Section 4.

### 3.3. Independent SED Analysis

We used the broadband, combined-light SED of the system, along with the Gaia DR2 parallax, iteratively with the global modeling to check for the possibility of any additional sources of light in the system beyond the four eclipsing components, AaAb+BaBb (Figure 8). This is separate to the analysis described in Section 3.2 and as such provided an independent check on the parameters found. We performed the independent SED modeling with the procedures that

<sup>25</sup> <http://stev.oapd.inaf.it/cgi-bin/cmd>

<sup>26</sup> In the first round we assumed, as usual, that the four stars have the same age but we were unable to find consistent, co-eval solution. Therefore, we decided to allow different stellar ages. This problem will be discussed later.

Stassun & Torres (2016) developed for EBs, extended here to the case of two EBs simultaneously.

In brief, a combined-light SED model is calculated from four Kurucz atmospheres (Kurucz 1993), interpolated to the initial estimate values of the individual stellar  $T_{\text{eff}}$  and scaled by the initial estimate values of the stellar surface areas ( $4\pi R_{\star}^2$ ). We assume the metallicity identified in the best-fit models, [M/H]  $-0.37^{+0.10}_{-0.16}$  dex. The remaining free parameters of the fit are the extinction,  $A_V$ , which we limited to the maximum for the line of sight from the dust maps of Schlegel et al. (1998), and the overall flux normalization,  $F_{\text{bol,tot}}$ . We adopted the NUV magnitudes from Galaxy Evolution Explorer,  $BVgri$  magnitudes from the AAVSO Photometric All-Sky Survey (APASS) catalog, the  $JHK_S$  magnitudes from 2MASS, the W1–W4 magnitudes from the Wide-field Infrared Survey Explorer (WISE), and the  $GG_{BP}G_{RP}$  magnitudes from Gaia. Together, the available photometry spans the full stellar SED over the wavelength range 0.2–22  $\mu\text{m}$  (see Figure 8).

The resulting fit is excellent (Figure 8) with a reduced  $\chi^2 = 1.2$  and  $A_V = 0.22^{+0.00}_{-0.02}$  (i.e., the maximum permitted  $A_V$  for the line of sight from the dust maps of Schlegel et al. (1998), which is expected for the nominal system distance). The total (unextincted)  $F_{\text{bol,tot}}$  obtained from the observed photometry, together with the model inferred bolometric luminosity ( $L_{\text{bol,tot}} \equiv 4\pi\sigma_{\text{SB}}\Sigma R_{\star}^2 T_{\text{eff}}^4$ ), yields an implied photometric distance of  $964 \pm 13$  pc.

This is consistent with the model in Section 3.2 ( $d_{\text{model}} = 958^{+23}_{-23}$  pc) and confirms that the system is likely to be further away than the uncorrected Gaia parallax indicates ( $d_{\text{Gaia}} = 928 \pm 12$  pc).

## 4. Discussion

### 4.1. Examining the Model

As demonstrated in Section 2.6, by comparison with other work, the age constraints from the Li I EW are 10–50 Myr. The ages (with uncertainties) of Aa, Ba, and Bb in Table 3 are consistent with this.

The uncertainties in the masses of the four stars may appear to be remarkably low. The combined analysis described in Section 3.2 returns mass ratios, fractional radii, and fractional luminosity, as indicated in Table 3. The mass of one star is required as an input parameter. As discussed in Section 3.2, the mass of Aa was allowed to adjust with the use of a simple uniform prior. The uncertainty in the mass of Aa reflects the “cloud” of solutions which were consistent with the data derived from TESS observations, the ETV analysis, the RVs, the SED, data from Gaia, and the extinction. Stellar evolutionary codes are used to confirm that the ages indicated by the physical quantities of the four stars are consistent with the ages indicated by the Li I EW. A wide range of metallicity is indicated, but the stars are clearly sub-solar.

PARSEC evolutionary tracks for the four components of TIC 27895647 from the best-fit model are presented in Figure 9. This  $T_{\text{eff}}$  versus  $\log g$  plot indicates the position of the best-fit models, with uncertainties, with color representing age. As indicated in Table 3, the ages are different: Aa is the youngest at  $10.0^{+0.7}_{-1.1}$  Myr, Ab the oldest at  $79.4^{+13.9}_{-11.8}$  Myr, while Ba and Bb have the same age at  $50.1^{+6.2}_{-11.2}$  Myr. Ab is the only star in Table 3 to have an age which is inconsistent with the Li I EW.

We obtained MESA stellar tracks for the minimum, median, and maximum masses indicated by the PARSEC isochrones at  $Z = 0.01$ . While this metallicity is not identical to the best fit, it

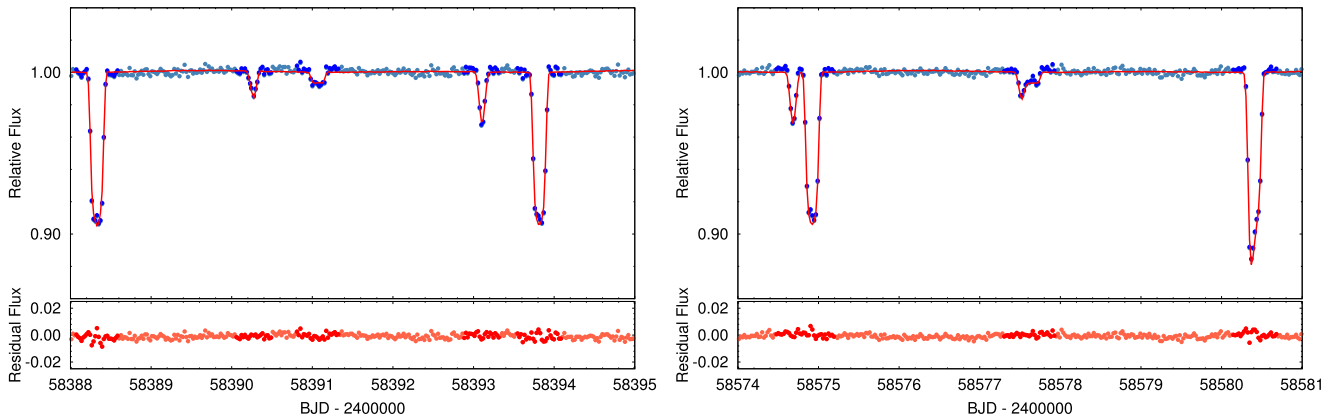


**Figure 7.** Two 7 day-long sections of the TESS Year 1 lightcurve of TIC 278956474. Instead of the full resolution-detrended Presearch Data Conditioning Simple Aperture Photometry two-minute cadence flux curve, we plot the 1800 s binned lightcurve which was used for the photodynamical analysis (see the text for details). The dark blue circles in the  $\pm 0.4$  phase-domain around each individual minimum represent the 1800 s binned flux values used for the photodynamical model, while the other out-of-eclipse data (not used in the modeling) are plotted as light blue circles. The red curve is the cadence-time-corrected photodynamical model solution (see Section 3.2); the residuals to the model are also shown in the bottom panels. Left panel: here the four different types of eclipse are well separated. From left to right one can see primary eclipse of binary A, secondary of binary B, secondary of binary A, primary of binary B and, finally, the next primary eclipse of binary A. The right panel illustrates the superpositions of both the secondary (in the middle) and the primary eclipses (to the right) of the two binaries.

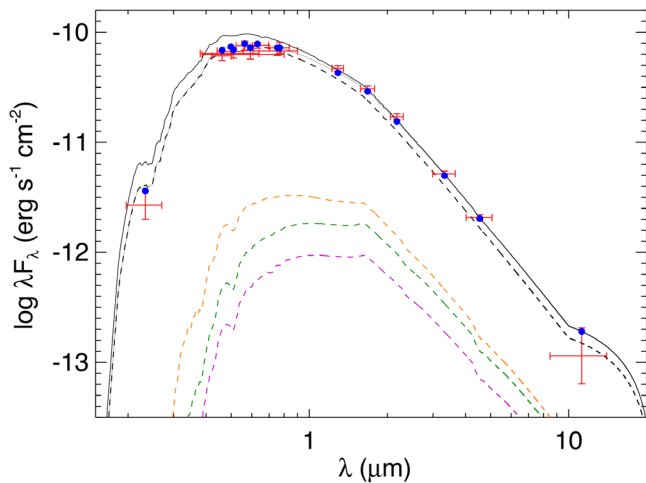


**Figure 8.** Spectral energy distribution. Red symbols represent the observed photometric measurements, where the horizontal bars represent the effective width of the passband. Blue symbols are the model fluxes from the best-fit combined Kurucz atmosphere model (black solid, without extinction; gray, with extinction). Each of the four stellar components is represented by a Kurucz atmosphere of a different color, scaled by the relative stellar surface areas. Black dashed: Aa. Purple: Ab. Orange: Ba. Green: Bb.

is well within the uncertainty. We match the parameters for Aa at  $14 \pm 2$  Myr, a good approximation with the PARSEC tracks given the small difference in metallicity. This is consistent with the Li I EW age.

In Figure 10 we compare properties of stars with an initial mass matching the minimum (green), median (blue), and maximum (red) masses from Table 3. It appears from panel (b) (core temperature), panel (c) (core density), and panel (d) (core pressure) that  $14 \pm 2$  Myr is approximately the point at which a star of the mass and metallicity of Aa would join the main sequence (ZAMS). The feature in panel (a) (radius), where Aa expands and then contracts at 10–20 Myr, is also evident in the PARSEC isochrones (Figure 9), where  $T_{\text{eff}}$  is plotted against  $\log g$ . Ab, Ba, and Bb would appear to be PMS stars.

The model of Ab is the only one that, from Table 3, does not have an age consistent with the Li I EW. The ratio of radii of

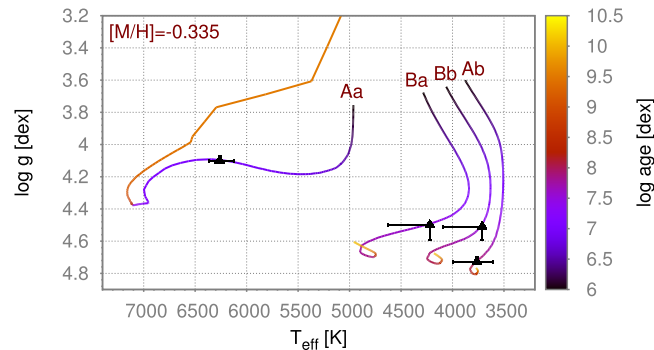


**Figure 9.**  $T_{\text{eff}}$  vs.  $\log g$  PARSEC evolutionary tracks for the four components of TIC 27895647 according to the best-fit model. The color scale denotes the age ( $\log \tau$ ) of the stars at any point along their evolution tracks. Black triangles mark the present locations of the four stars in the solution. We note that these positions, probably unphysically, belong to different ages of the given evolutionary tracks.

Aa and Ab is strongly constrained by the TESS data. From panel (a) in Figure 10, this points to a lower mass for Ab. Further spectroscopy is required to resolve this issue.

We see no evidence, such as infrared excess in the SED, of a disk in this system, which would appear to be consistent with Aa being at ZAMS rather than still in the T Tauri phase. Our estimate of  $E(B - V)$  is consistent with estimates of  $N_{\text{H,tot}}$  based on Swift data (Section 2.4, Willingale et al. 2013), although higher than other catalog values.

#### 4.2. Dynamical Properties of the Quadruple

From the joint light curve, ETV, and RV analysis TIC 278956474 was found to be one of the most compact known  $2 + 2$  quadruple stellar systems. We display the spatial configuration of the system in Figure 11. The median period of the outer orbit was found to be  $P_{\text{out}} = 858_{-5}^{+7}$  days, with a moderate eccentricity of  $e_{\text{out}} = 0.36_{-0.03}^{+0.02}$ . (For comparison, note that the tightest known  $2 + 2$  quadruple system, VW LMi, has an outer period of  $P_{\text{out}} = 355$  days and eccentricity of  $e_{\text{out}} < 0.1$ ; see Pribulla et al. 2008, 2020.) One should keep in mind, however, that while the bound quadruple nature of the system is certainly beyond question, the quantitative results on

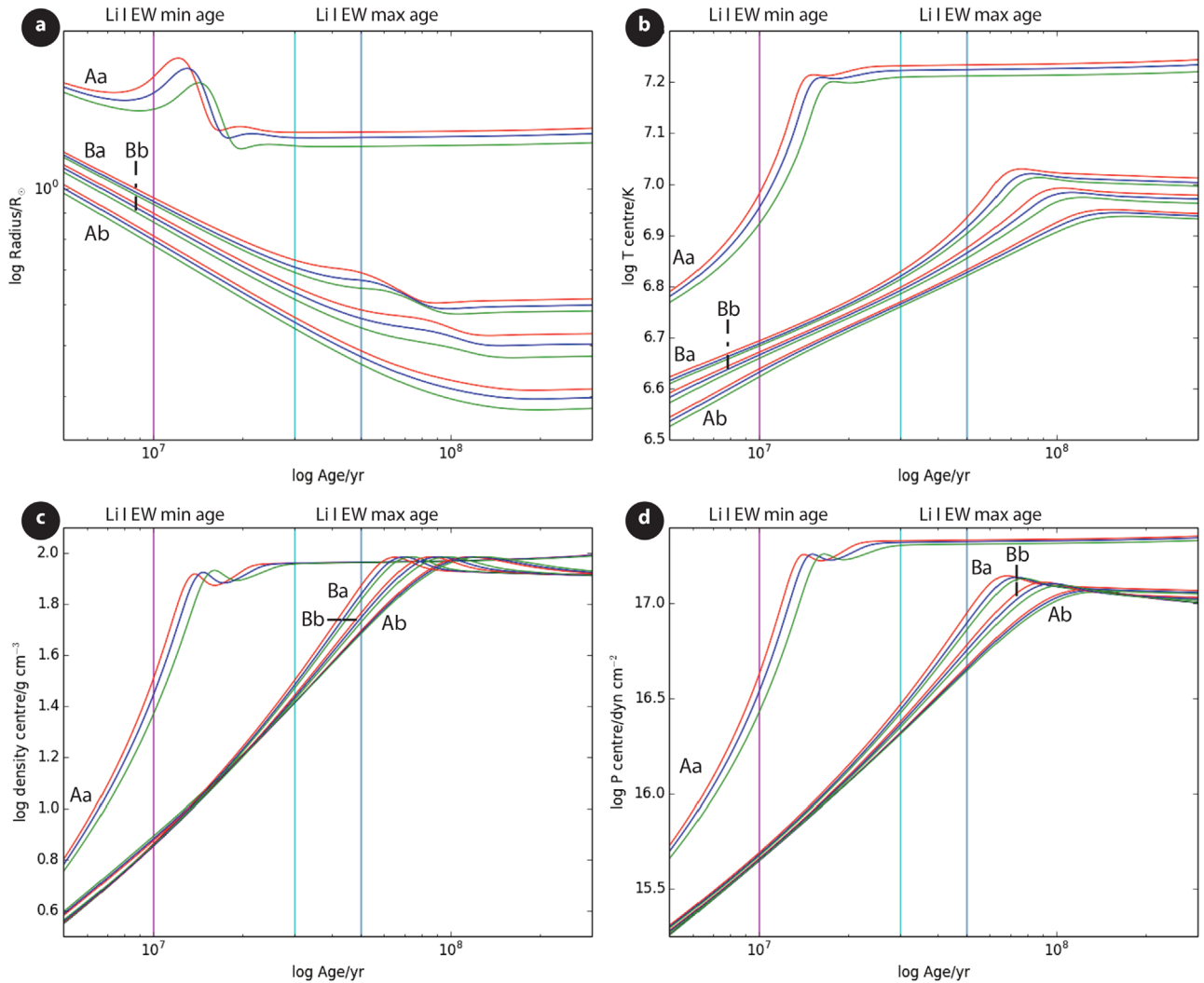


**Figure 10.** MESA isochrones,  $Z = 0.01$ , for the median (blue), minimum (green), and maximum (red) masses of the four stars from Table 3. The tracks for each star are labeled in each panel. The Li I EW indicates an age between 10 and 50 Myr, and these limits are also indicated on each panel, along with an age of 30 Myr. Panel (a): stellar radius (log scale) from  $0.33$  to  $2.00 R_{\odot}$ ; panel (b): core temperature; panel (c): core density; panel (d): core pressure. The point where each star joins the main sequence can be identified from the core characteristics. In these isochrones, which are at a slightly different metallicity to Table 3 (although within the error bars), the median parameters of Aa are matched at an age of  $14 \pm 2$  Myr, at about the same time, in these stellar tracks, as Aa joins the main sequence.

the orbital parameters of the outer orbit should be considered only with caution. The reason is that the TESS observations cover only a fraction of an outer orbital period and, furthermore, the four former, seasonal WASP minima have large uncertainties. Furthermore, as one can see in Figure 11, the present solution suggests that the system was observed around the apastron phase of the outer orbit, i.e., when the orbital motion is slowest and, therefore, the curvatures of ETVC curves are also minimized. Therefore, future follow-up eclipse timing observations would be extremely useful to obtain more certain outer orbital parameters.

In contrast to the outer orbit, the obtained elements of the two close binary orbits should be robust. The period ratio of the two binary orbits ( $P_B/P_A \sim 1.03$ ) is very close to unity. According to the results of Zasche et al. (2019) there is a significant excess of  $2+2$  quadruple systems with near-equal inner periods; however, the origin of this feature is still unknown (see also Breiter & Vokrouhlický 2018; Tremaine 2020). Turning to the other orbital parameters, as preliminary runs implied that eccentricities of both inner orbits should be less than 0.001, we assumed circular orbits for the subsequent analysis. This

assumption does not contradict the young age of the system, as it was shown by Zahn & Bouchet (1989) that the orbits of close binaries formed by late-type stars and having period  $P \lesssim 7-8$  days are expected to circularize by the end of the very first million years of their PMS evolution.

Regarding the binary–binary mutual (gravitational) interactions, their period and amplitude can be estimated from the analytical theory of the perturbations in hierarchical triple systems (see, e.g., Soderhjelm 1975). The key parameter is the period ratio of  $P_{\text{out}}/P_{\text{in}}$  which is  $\approx 150$  for both binaries. According to the results of Borkovits et al. (2015, 2016), for such a high value the short-term perturbations are negligible and, therefore, within the timescale of the  $\sim 1$  year-long TESS observations, the orbital motion of the four stars along their inner and outer orbits can be considered as unperturbed Keplerian motions. As a consequence, neither the TESS photometry nor the RV measurements carry any information about the nodal angles of the three orbital planes and, therefore, despite the fact that the angles of inclination of A ( $i_A = 88.97^{+0.16}_{-0.19}$  deg) and B ( $i_B = 89.23^{+0.16}_{-0.08}$  deg), and also of the outer orbit ( $i_{\text{out}} = 85^{+3}_{-2}$  deg) were found to be very

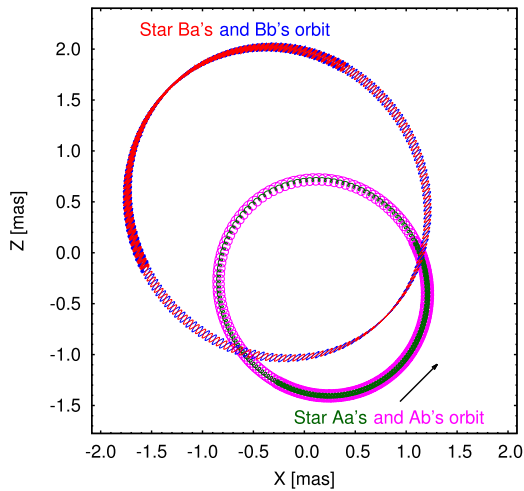


**Figure 11.** Spatial revolutions of the four members of TIC 278956474, during an outer period, projected to the  $x - z$  plane where the observer is located toward the negative  $z$  direction, while the  $x$  axis represents the intersection of the orbital plane of the outer orbit with the tangential plane of the sky. The thick arcs represent the four stars’ motion during the 11 month-long observations of the TESS spacecraft. The black arrow shows the direction of the revolution along the outer orbits. The center of mass of the quadruple system is located at the point (0, 0). Note that, in the absence of any information about the nodes of the three orbital planes, we assumed quite arbitrarily in this figure that all three orbital planes intersect the tangential plane of the sky in the same line (i. e.  $\Omega_A = \Omega_B = \Omega_{out}$ ).

similar, one cannot declare that the orbits are almost coplanar. In contrast, one can say nothing about the mutual inclinations of any two of three orbital planes.<sup>27</sup>

Considering the larger amplitude, so-called apse-node time-scale (or secular) perturbations, their characteristic period is proportional to  $P_{out}^2/P_{in} \approx 350$  yr for our quadruple. In this way, in the case of a non-coplanar configuration, we can expect significant inclination and therefore well-observable eclipse depth variations within a few decades.

### 4.3. Young Quadruple Systems

From the Li I EW (Section 2.6), this quadruple system is young (10–50 Myr). In Section 1 we referred to Marks & Kroupa (2012), who demonstrated through simulations that if a cluster started with a formal binary fraction of unity, the binary fraction would reduce over time to match currently observed values. Our analysis of this system indicates that even small groupings of stars may form as hierarchical multiples. Whether systems such as TIC 278956474 are likely to become unbound over time would be an interesting follow-up study.

Of the young quadruple systems mentioned in Section 1, some are young enough to be consistent with T Tauri stars. GG Tauri and HD 98800, for example, have evidence of circumbinary discs around one of the inner binaries (Guilloteau et al. 1999; Koerner et al. 2000; Ribas et al. 2018), as well as periods significantly longer than that of TIC 278956474. The inner binaries in GG Tauri have periods of  $\approx 403$  days and 40,000 yr (Köhler 2011), while the inner binaries of HD 98800 have periods of about 315 days (Ribas et al. 2018 and references therein). The inner period of HD 34700 has been measured at 23.5 days (Torres 2004; Sterzik et al. 2005).

<sup>27</sup> Strictly speaking, what we can obtain uniquely is only  $\sin i$ , therefore even these three inclination values are ambiguous for the undetermined signs of  $\cos i$ -s.

Again, there is evidence of a circumstellar disk (Seok & Li 2015). We have no evidence of a circumstellar disk around TIC 278956474, nor would we expect to find any in a system where the brightest star is at ZAMS.

LkCa 3 is a young quadruple system, with an age of about 1.4 Myr (Torres et al. 2013) where all four components are M-class stars. This is interesting as it is generally accepted that high-mass stars are more likely to be binary than are low-mass stars. Our final model of TIC 278956474 suggests that, while the spectral classes of the stars will eventually be F3 (Aa), M0 (Ab), K3 (Ba), and K7 (Bb), currently both Ab and Bb could be considered M-class.

González et al. (2006) report the age of AO Vel to be ZAMS, with two short-period inner binaries: 1.58 and 4.15 days. The outer period is reported as 41.0 yr. This system is listed on Simbad as an Algol-type EB. The inner periods of AO Vel are shorter than those of TIC 278956474, but do not share the characteristic of being very similar in duration.

Wolter et al. (2014) revisited the age of the quadruple system AB Doradus (as opposed to the moving group of the same name), and concluded that it is 50–100 Myr old. This is older than TIC 278956474 and the periods are longer. One inner binary has a period of 11.7 yr, the other has a period of 361 days, and the outer period is estimated at  $\approx 1500$  yr (Wolter et al. 2014).

HD 91962 is unusual in that three companions appear to orbit one central star (Tokovinin et al. 2015). The system is considered to be young on the basis of lithium abundances, and the three periods are 170.3 days, 8.85 yr, and 205 yr. Tokovinin et al. (2015) put forward the theory that this system was formed when companions migrated in a dissipative disk formed from the collapse of an isolated core. TIC 278956474 may also have formed from the collapse of an isolated core, but has a more conventional architecture.

HD 86588 is dated to  $10 \lesssim \text{Myr} \lesssim 150$  (Tokovinin et al. 2018) and therefore overlaps in terms of age with TIC 278956474, although not in architecture. The four stars, with masses  $1 \lesssim M/M_{\odot} \lesssim 1.3$ , are in a three-tier hierarchy. The inner period, 2.4058 days, has not yet fully circularized as the eccentricity is  $0.086 \pm 0.003$ . By contrast, in TIC 278956474 the two inner periods have circularized. Tokovinin et al. (2018) state the outermost period of HD 86588 to be around 300 yr, and that the intermediate period is 8 yr.

Young quadruple systems come in many guises, and TIC 278956474 adds to our understanding of such systems. Both inner periods are known to be short, are circularized, and are similar in duration to each other. HD 34700 also has a short inner period. AO Vel also has two short-period inner binaries, but one inner period is  $\approx 2.6$  times as long as the other. The inner period of HD 86588 is shorter than in TIC 278956474 but has not yet circularized: both inner periods in TIC 278956474 are already circular. The other young quadruple systems tend toward longer inner periods.

In terms of architecture, as a 2 + 2 quadruple system TIC 278956474 is similar to most other known young quadruple systems. Other architectures are observed, but appear to be less common.

Of the eight systems other than TIC 278956474 discussed here, HD 98800 appears to have no entry in Gaia DR2, but has a known distance of 47 pc (Soderblom et al. 1998). LkCa3 has no parallax recorded in Gaia DR2 but has a known distance of 133 pc (Torres et al. 2013). GG Tauri has a negative parallax in

Gaia DR2, but has a known distance of 140 pc (Brauer et al. 2019 and references therein). The remaining systems all have reliable parallaxes in Gaia DR2. AB Doradus ( $65.3 \pm 0.1$  mas), HD 91962 ( $28.2 \pm 0.5$  mas), and HD 34700 ( $2.81 \pm 0.05$  mas) all have parallaxes indicating they are closer to us than is TIC 278956474. AO Vel ( $1.12 \pm 0.04$  mas) and HD 86588 ( $1.00 \pm 0.05$  mas) have a similar parallax to, and hence are at about the same distance as, TIC 278956474. None appears to be significantly further away.

Because of its magnitude and distance, without TESS observations and the SPOC pipeline processing, TIC 278956474's nature as a quadruple system, rather than a single star, would not have been identified.

## 5. Conclusion

The TESS mission has enabled the identification of TIC 278956474 as a 2+2 quadruple system composed of two short-period EBs, where all previous observations, including Gaia, indicated that this system was a single star.

The eclipses detected in the SPOC pipeline cannot be planetary in nature. Aa and Ab have the same period as each other, as do Ba and Bb. The periods of Aa+Ab and of Ba+Bb, 5.488 days and 5.674 days respectively, would not appear to be consistent with a stable planetary system. While highly inflated short-period planets can have secondaries, the eclipses of both Ab and Bb are too deep for this to be a reasonable explanation.

Using SPOC data validation reports, archival WASP-South data, a study of ETVs, speckle photometry, spectroscopy, data from Gaia DR2, and the BiSEPS, MESA and PARSEC stellar evolutionary codes, we identified a model for the four stars in this system which is consistent with observations, the SED and the uncorrected Gaia parallax. It is unlikely that there are additional detectable components. The best-fit parameters are given in Table 3.

The Li I EW indicates an age of 10–50 Myr, and our model is consistent with this approximation. One star appears to be at ZAMS, while the other three are still on the PMS.

Further observations, in particular spectroscopy and photometry, would be valuable in refining the properties of this system,

in particular the parameters of the outer period (Figure 11). The system will be re-observed by TESS in Sectors 27-39 (cycle 3).

The authors thank the anonymous referee for his or her helpful comments.

This paper includes data collected by the TESS mission, which are publicly available from the Mikulski Archive for Space Telescopes (MAST). Funding for the TESS mission is provided by NASA's Science Mission directorate.

Resources supporting this work were provided by the NASA High-End Computing (HEC) Program through the NASA Advanced Supercomputing (NAS) Division at Ames Research Center for the production of the SPOC data products.

This work has made use of data from the European Space Agency (ESA) mission Gaia (<https://www.cosmos.esa.int/gaia>), processed by the Gaia Data Processing and Analysis Consortium (DPAC, <https://www.cosmos.esa.int/web/gaia/dpac/consortium>). Funding for the DPAC has been provided by national institutions, in particular the institutions participating in the Gaia Multilateral Agreement.

T.B. acknowledges the financial support of the Hungarian National Research, Development and Innovation Office—NKFIH grant KH-130372.

The authors also thank Oleg Khozhura for his contribution to this paper.

*Software:* BiSEPS (Willems & Kolb 2002, 2004; Willems et al. 2006; Davis et al. 2010; Farmer et al. 2013), gnuplot (<http://www.gnuplot.info/>), Lightcurvefactory (Borkovits et al. 2018, 2019b), MESA (Paxton et al. 2011, 2013, 2015), PARSEC (Bressan et al. 2012), Wotan (Hippke et al. 2019).

## Appendix A SPOC Data

Table A1 presents selected data from all the single-sector and multi-sector data validation reports hosted on MAST, as well as the additional science run for sectors 1-13 (denoted with an asterisk).

**Table A1**  
Data from SPOC

Component	Sector	Period (days)	Depth (ppm)	Duration (hr)	Ingress (hr)	Odd depth (ppm)	Even depth (ppm)	Secondary depth (ppm)
Aa	1	$5.4881 \pm 0.0002$	$94800 \pm 900$	$5.50 \pm 0.04$	$1.22 \pm 0.04$	$94000 \pm 1000$	$96000 \pm 1000$	Component Ab
Aa	1–2	$5.48797 \pm 0.00008$	$94600 \pm 600$	$5.44 \pm 0.03$	$1.21 \pm 0.02$	$95100 \pm 900$	$94500 \pm 800$	Component Ab
Aa	1–3	$5.48789 \pm 0.00004$	$94200 \pm 500$	$5.43 \pm 0.02$	$1.21 \pm 0.02$	$93900 \pm 600$	$94500 \pm 600$	Component Ab
Aa	1–6	$5.48797 \pm 0.00002$	$93900 \pm 300$	$5.41 \pm 0.01$	$1.20 \pm 0.01$	$95700 \pm 500$	$92900 \pm 500$	Component Ab
Aa	1–9	$5.487995 \pm 0.000008$	$94200 \pm 300$	$5.43 \pm 0.01$	$1.21 \pm 0.01$	$94400 \pm 400$	$94000 \pm 400$	Component Ab
Aa	1–13	$5.488035 \pm 0.000005$	$93900 \pm 200$	$5.43 \pm 0.01$	$1.22 \pm 0.01$	$94600 \pm 300$	$93300 \pm 300$	$8900 \pm 400$
Aa	1–13*	$5.488036 \pm 0.000005$	$93900 \pm 200$	$5.43 \pm 0.01$	$1.22 \pm 0.01$	$94500 \pm 300$	$93400 \pm 300$	Component Ab
Aa	2	$5.4878 \pm 0.0002$	$94700 \pm 900$	$5.42 \pm 0.03$	$1.22 \pm 0.03$	$94000 \pm 1000$	$97000 \pm 2000$	Component Ab
Aa	3	$5.4882 \pm 0.0003$	$93700 \pm 600$	$5.43 \pm 0.03$	$1.20 \pm 0.03$	$94300 \pm 800$	$92400 \pm 900$	Component Ab
Aa	4	$5.4882 \pm 0.0003$	$93400 \pm 800$	$5.34 \pm 0.04$	$1.18 \pm 0.04$	$98000 \pm 1000$	$91000 \pm 1000$	Component Ab
Aa	5	$5.4884 \pm 0.0003$	$94300 \pm 800$	$5.47 \pm 0.03$	$1.24 \pm 0.03$	$94000 \pm 1000$	$95000 \pm 1000$	Component Ab
Aa	6	$5.4881 \pm 0.0003$	$95700 \pm 800$	$5.41 \pm 0.03$	$1.21 \pm 0.03$	$96000 \pm 1000$	$96000 \pm 1000$	Component Ab
Aa	7	$5.4877 \pm 0.0002$	$93000 \pm 1000$	$5.38 \pm 0.04$	$1.21 \pm 0.03$	$88000 \pm 2000$	$97000 \pm 2000$	$7000 \pm 2000$
Aa	8	$5.4873 \pm 0.0002$	$93000 \pm 1000$	$5.46 \pm 0.03$	$1.21 \pm 0.03$	$56378 \pm 1000$	$95147 \pm 2000$	Component Ab
Aa	9	$5.4888 \pm 0.0003$	$93400 \pm 900$	$5.45 \pm 0.03$	$1.27 \pm 0.03$	$94000 \pm 1000$	$93293 \pm 1000$	Component Ab
Aa	10	$5.4890 \pm 0.0003$	$93600 \pm 700$	$5.53 \pm 0.04$	$1.31 \pm 0.04$	$98000 \pm 1000$	$90000 \pm 1000$	Component Ab
Aa	11	$5.4885 \pm 0.0003$	$92100 \pm 800$	$5.41 \pm 0.04$	$1.20 \pm 0.04$	$91000 \pm 1000$	$93000 \pm 1000$	Component Ab
Aa	12	$5.4880 \pm 0.0003$	$95000 \pm 1000$	$5.42 \pm 0.04$	$1.2 \pm 0.04$	$95000 \pm 2000$	$94000 \pm 2000$	Component Ab
Aa	13	$5.4882 \pm 0.0003$	$94000 \pm 1000$	$5.43 \pm 0.04$	$1.21 \pm 0.04$	$94000 \pm 2000$	$94000 \pm 2000$	$8000 \pm 2000$

**Table A1**  
(Continued)

Component	Sector	Period (days)	Depth (ppm)	Duration (hr)	Ingress (hr)	Odd depth (ppm)	Even depth (ppm)	Secondary depth (ppm)
Ab	1	5.495 ± 0.003	8500 ± 800	5.5 ± 0.4	1.1 ± 0.4	8000 ± 30000	8000 ± 1000	Component Aa
Ab	1–2	5.4883 ± 0.0008	9100 ± 600	5.3 ± 0.2	1.1 ± 0.2	8900 ± 800	8300 ± 800	Component Aa
Ab	1–3	5.4881 ± 0.0004	9100 ± 400	5.3 ± 0.2	1.0 ± 0.2	9400 ± 500	8200 ± 600	Component Aa
Ab	1–6	5.4882 ± 0.0001	9000 ± 300	5.3 ± 0.1	0.9 ± 0.1	9300 ± 400	8400 ± 400	Component Aa
Ab	1–9	5.48809 ± 0.00007	8900 ± 200	5.4 ± 0.1	1.1 ± 0.1	9200 ± 300	8600 ± 400	Component Aa
Ab	1–13	2.74403 ± 0.00002	8900 ± 200	5.29 ± 0.09	1.0 ± 0.1	Model fitter failed	Model fitter failed	n/a
Ab	1–13*	5.48808 ± 0.00004	8900 ± 200	5.29 ± 0.08	1.0 ± 0.1	9000 ± 300	8700 ± 300	Component Aa
Ab	2	5.488 ± 0.002	9700 ± 700	5.2 ± 0.2	1.0 ± 0.3	9900 ± 900	9000 ± 1000	Component Aa
Ab	3	10.977 ± 0.004	9155 ± 600	5.0 ± 0.3	0.4 ± 0.3	9600 ± 900	8700 ± 900	Component Aa
Ab	4	5.482 ± 0.002	7700 ± 700	4.9 ± 0.3	0.4 ± 0.3	8000 ± 1000	8000 ± 1000	Component Aa
Ab	5	5.488 ± 0.002	9500 ± 600	5.5 ± 0.2	1.4 ± 0.3	8200 ± 700	10100 ± 800	Component Aa
Ab	6	5.489 ± 0.002	9600 ± 700	4.9 ± 0.2	0.6 ± 0.2	10000 ± 1000	9000 ± 1000	Component Aa
Ab	8	5.492 ± 0.002	7600 ± 900	4.2 ± 0.3	0.4 ± 0.3	8000 ± 1000	8000 ± 800	Component Aa
Ab	9	5.489 ± 0.001	8900 ± 600	5.1 ± 0.2	0.4 ± 0.2	9300 ± 700	8500 ± 800	Component Aa
Ab	10	5.488 ± 0.002	9002 ± 700	5.1 ± 0.3	0.8 ± 0.3	9500 ± 700	7000 ± 1000	Component Aa
Ab	11	5.485 ± 0.001	8000 ± 500	5.0 ± 0.3	0.6 ± 0.3	8400 ± 800	800 ± 800	Component Aa
Ab	12	5.485 ± 0.002	9600 ± 800	5.0 ± 0.3	0.8 ± 0.3	10000 ± 1000	10000 ± 1000	Component Aa
B	1–6	2.83721 ± 0.00002	26000 ± 300	3.34 ± 0.04	1.67 ± 0.02	16700 ± 400	33900 ± 400	n/a
B	1–9	2.83718 ± 0.00001	25400 ± 300	3.34 ± 0.04	1.67 ± 0.02	16700 ± 300	33500 ± 300	n/a
B	1–13	2.837163 ± 0.000007	25100 ± 200	3.34 ± 0.03	1.67 ± 0.02	16400 ± 300	33400 ± 300	n/a
B	1–13*	2.837162 ± 0.000007	25100 ± 200	3.34 ± 0.03	1.67 ± 0.02	16400 ± 200	33400 ± 300	n/a
B	3	2.8372 ± 0.0004	28400 ± 700	3.3 ± 0.1	1.65 ± 0.05	34400 ± 900	17000 ± 1000	n/a
B	4	2.8366 ± 0.0004	23700 ± 800	3.3 ± 0.1	1.63 ± 0.06	18600 ± 900	33000 ± 1000	n/a
B	5	2.8373 ± 0.0003	26500 ± 600	3.31 ± 0.08	1.65 ± 0.04	33800 ± 700	15800 ± 800	n/a
B	8	2.8370 ± 0.0003	23000 ± 1000	3.4 ± 0.1	1.71 ± 0.06	31000 ± 1000	17000 ± 1000	n/a
B	9	2.8369 ± 0.0003	23400 ± 700	3.3 ± 0.1	1.66 ± 0.05	16600 ± 900	32600 ± 900	n/a
B	11	2.8371 ± 0.0003	23800 ± 700	3.3 ± 0.1	1.63 ± 0.05	32300 ± 800	16400 ± 900	n/a
Ba	1	5.6742 ± 0.0009	37000 ± 1000	3.4 ± 0.1	1.70 ± 0.05	39000 ± 2000	34000 ± 2000	15000 ± 1000
Ba	1–2	5.6744 ± 0.0002	35000 ± 700	3.32 ± 0.07	1.66 ± 0.04	36800 ± 900	33000 ± 2000	Component Bb
Ba	1–3	5.6744 ± 0.0001	34700 ± 500	3.29 ± 0.06	1.65 ± 0.03	35600 ± 700	33600 ± 800	Component Bb
Ba	2	5.6742 ± 0.0007	33000 ± 1000	3.21 ± 0.09	1.60 ± 0.04	33000 ± 1000	34000 ± 1000	Component Bb
Ba	6	5.6745 ± 0.0007	32600 ± 900	3.38 ± 0.09	1.69 ± 0.05	33000 ± 2000	33000 ± 1000	Component Bb
Ba	7	5.6736 ± 0.0007	33000 ± 1000	3.3 ± 0.1	1.64 ± 0.05	33000 ± 1000	34000 ± 1000	Component Bb
Ba	12	5.6740 ± 0.0008	36000 ± 1000	3.3 ± 0.1	1.67 ± 0.05	35000 ± 2000	36000 ± 2000	Component Bb
Ba	13	5.671 ± 0.0008	34000 ± 1000	3.3 ± 0.1	1.65 ± 0.06	36000 ± 2000	33000 ± 2000	2300 ± 900
Bb	1–2	5.6742 ± 0.0006	15800 ± 600	3.3 ± 0.2	1.64 ± 0.08	15000 ± 1000	16600 ± 900	Component Ba
Bb	1–3	5.6747 ± 0.0003	16000 ± 600	3.4 ± 0.2	1.67 ± 0.07	15000 ± 1000	16600 ± 700	Component Ba
Bb	2	5.675 ± 0.001	14900 ± 900	3.3 ± 0.2	1.64 ± 0.1	16000 ± 2000	14000 ± 1000	Component Ba
Bb	6	5.675 ± 0.001	16500 ± 700	3.3 ± 0.2	1.66 ± 0.09	18000 ± 1000	15000 ± 1000	Component Ba
Bb	7	2.836 ± 0.003	15000 ± 2000	3.3 ± 0.3	1.6 ± 0.2	Model fitter failed	Model fitter failed	n/a
Bb	10	5.6754 ± 0.0009	15400 ± 800	3.2 ± 0.2	1.6 ± 0.1	17000 ± 1000	14000 ± 1000	2331.4 ± 600
Bb	12	5.6724 ± 0.0001	17000 ± 1000	3.1 ± 0.2	1.5 ± 0.1	15000 ± 2000	18000 ± 2000	Component Ba

**Note.** The secondary in component Aa coincides with the time of the primary in component Ab, and vice versa. Similarly for components Ba and Bb. Secondary depths are therefore only included where each component is not separately identified. A second science run was completed for multisector 1–13 in order to identify component Ab at the correct period and to remove the partial eclipse of Aa at the end of sector 8. This science run is identified as sector 1–13\*.

## Appendix B ETV Tables

Minima times for binary A (Table B1) and binary B (Table B2). Note that the four WASP-South data points in

Table B1 are seasonal (Section 2.3), while the remaining data points are based on individual TESS events.

**Table B1**  
Times of Minima of TIC 278956474A

BJD (−2,400,000)	Cycle no.	std. dev. ( <i>d</i> )	BJD (−2,400,000)	Cycle no.	std. dev. ( <i>d</i> )	BJD −2,400,000	Cycle no.	std. dev. ( <i>d</i> )
54826.636808	−638.0	0.000549	58445.944896	21.5	0.001468	58572.167299	44.5	0.000979
55194.333657	−571.0	0.001098	58448.697063	22.0	0.000144	58574.921743	45.0	0.000141
55562.031003	−504.0	0.001098	58454.185939*	23.0	0.000128	58577.656449	45.5	0.000872
55924.227778	−438.0	0.001098	58456.919263	23.5	0.001334	58580.409879	46.0	0.000133
58327.962429	0.0	0.000174	58459.673021	24.0	0.000130	58585.899280*	47.0	0.000168
58330.700768	0.5	0.002383	58462.411516	24.5	0.002015	58588.633820	47.5	0.001724
58333.449810	1.0	0.000223	58470.649037	26.0	0.000121	58591.386912	48.0	0.000130
58336.192167	1.5	0.001068	58473.389849	26.5	0.001229	58594.119542	48.5	0.000951
58341.672992	2.5	0.002330	58476.136447	27.0	0.000126	58599.627581	49.5	0.004254
58344.425319	3.0	0.000195	58478.879249	27.5	0.001043	58602.362426	50.0	0.000175
58347.162986	3.5	0.001927	58481.624776	28.0	0.000129	58605.100888	50.5	0.001569
58349.913744	4.0	0.000150	58484.363435	28.5	0.000751	58607.850858	51.0	0.000153
58352.658427	4.5	0.003649	58487.112762	29.0	0.000132	58613.338684	52.0	0.000178
58355.401627	5.0	0.000131	58489.871693	29.5	0.001835	58616.075255	52.5	0.001549
58358.135368	5.5	0.000848	58492.600453	30.0	0.000156	58618.827111	53.0	0.000147
58360.890011	6.0	0.000140	58495.332830	30.5	0.001338	58621.561695	53.5	0.002102
58363.626999	6.5	0.000658	58498.091166*	31.0	0.000114	58627.044601	54.5	0.001205
58366.377135	7.0	0.000161	58500.833321	31.5	0.001364	58629.803406	55.0	0.000155
58369.122007	7.5	0.001326	58506.312484	32.5	0.001090	58632.542077	55.5	0.000921
58371.864689	8.0	0.000139	58509.064706	33.0	0.000139	58635.290572	56.0	0.000146
58374.600726	8.5	0.001342	58511.819107	33.5	0.001813	58638.019856	56.5	0.001641
58377.352284	9.0	0.000176	58514.552784	34.0	0.000109	58640.779257	57.0	0.000178
58380.083629	9.5	0.001641	58520.041266	35.0	0.000131	58643.516085	57.5	0.001110
58388.328366	11.0	0.000168	58522.785816	35.5	0.001032	58646.267602	58.0	0.000178
58391.068826	11.5	0.001415	58525.529251	36.0	0.000152	58648.989799	58.5	0.001197
58393.816827	12.0	0.000204	58528.268281	36.5	0.001249	58651.755432	59.0	0.000158
58399.305162	13.0	0.000119	58536.507117*	38.0	0.000140	58654.489005	59.5	0.001140
58402.042463	13.5	0.002526	58539.236620	38.5	0.002777	58657.244598	60.0	0.000171
58404.792220	14.0	0.000199	58541.983305*	39.0	0.000730	58659.983219	60.5	0.000950
58413.012446	15.5	0.001254	58544.732586	39.5	0.001435	58662.733098	61.0	0.000206
58415.768382	16.0	0.000163	58547.480518	40.0	0.000138	58665.481953	61.5	0.001844
58426.744932	18.0	0.000142	58550.226769	40.5	0.002788	58670.967933	62.5	0.001479
58429.484915	18.5	0.004152	58552.968752	41.0	0.000133	58673.708794	63.0	0.000138
58432.234014*	19.0	0.000134	58558.457413	42.0	0.000118	58676.450537	63.5	0.001335
58434.963124	19.5	0.002461	58561.201168	42.5	0.001212	58679.197053	64.0	0.000169
58440.456132	20.5	0.001355	58563.945780	43.0	0.000125	58681.947227	64.5	0.001120
58443.208790	21.0	0.000129	58566.683307	43.5	0.001859			

**Note.** The first four items give seasonal minima deduced from WASP-South observations. Other data refer to individual eclipses observed by TESS spacecraft. Integer and half-integer cycle numbers refer to primary and secondary eclipses. For the ETV analysis, discussed in the main part of the paper, only primary eclipses were used. Five primary eclipses marked with asterisks were omitted from the analysis as outliers.

**Table B2**  
Times of Minima of TIC 278956474B

BJD (−2,400,000)	Cycle no.	std. dev. ( <i>d</i> )	BJD −2,400,000	Cycle no.	std. dev. ( <i>d</i> )	BJD (−2,400,000)	Cycle no.	std. dev. ( <i>d</i> )
58327.851141	−0.5	0.001078	58452.679392	21.5	0.001835	58571.848064	42.5	0.004826
58330.686768	0.0	0.000472	58455.526205	22.0	0.000464	58574.684476	43.0	0.000540
58333.528644	0.5	0.024207	58458.360384	22.5	0.001879	58577.518764	43.5	0.000973
58336.361373	1.0	0.000515	58461.196935*	23.0	0.000365	58580.356649	44.0	0.000601
58342.033623*	2.0	0.000564	58464.050752	23.5	0.084498	58586.031380	45.0	0.000574
58344.876998	2.5	0.001018	58469.709234	24.5	0.000666	58588.873801	45.5	0.001518
58347.706677*	3.0	0.001567	58472.547953	25.0	0.000955	58591.706607	46.0	0.000473
58350.555515	3.5	0.001240	58475.388524	25.5	0.000929	58594.549605	46.5	0.000516
58356.227407	4.5	0.000779	58478.217404*	26.0	0.000962	58600.216707	47.5	0.001307
58359.060381	5.0	0.000372	58481.055791	26.5	0.001051	58603.056249	48.0	0.000425
58361.901701	5.5	0.000839	58483.891625*	27.0	0.000601	58605.887612	48.5	0.000994
58364.732752	6.0	0.000722	58486.738529	27.5	0.001463	58608.722728*	49.0	0.000537
58370.408184	7.0	0.000478	58489.570680	28.0	0.000380	58614.401286	50.0	0.000479
58373.248194	7.5	0.001198	58492.406297	28.5	0.001592	58617.242303	50.5	0.001257
58376.082783	8.0	0.000501	58495.246523	29.0	0.000561	58620.073963*	51.0	0.000724
58378.922654	8.5	0.001383	58498.085931	29.5	0.000965	58622.913595	51.5	0.001044
58387.429007*	10.0	0.000441	58500.914410*	30.0	0.000567	58625.754045	52.0	0.000944
58390.269093	10.5	0.003915	58506.594229	31.0	0.000351	58628.598291	52.5	0.001760
58393.105081	11.0	0.000456	58509.437963	31.5	0.001246	58631.428199	53.0	0.000505
58398.781892	12.0	0.000383	58512.267718	32.0	0.000517	58634.269473	53.5	0.001228
58401.621516	12.5	0.001218	58515.106161	32.5	0.000786	58637.101893	54.0	0.000492
58404.454889	13.0	0.000390	58517.935775*	33.0	0.000618	58642.776264	55.0	0.000615
58412.965130	14.5	0.001871	58520.781624	33.5	0.001152	58645.618682	55.5	0.000989
58415.799460*	15.0	0.000477	58523.616511	34.0	0.000617	58648.446307	56.0	0.000439
58421.478895	16.0	0.002228	58526.449138	34.5	0.000690	58651.283550	56.5	0.001568
58427.152712	17.0	0.000595	58537.802322	36.5	0.001126	58654.122005	57.0	0.000305
58429.994122	17.5	0.001210	58540.637289	37.0	0.000328	58656.962553	57.5	0.001599
58432.827096	18.0	0.000552	58546.311254	38.0	0.000428	58659.797199	58.0	0.001004
58435.667600	18.5	0.000915	58549.151810	38.5	0.000682	58662.627503	58.5	0.001251
58438.498776*	19.0	0.000330	58551.986126	39.0	0.000410	58665.470728	59.0	0.000598
58441.334196	19.5	0.001504	58554.816386	39.5	0.001820	58671.145005	60.0	0.000736
58444.173601*	20.0	0.000600	58560.498489	40.5	0.000809	58673.988971	60.5	0.001242
58447.015592	20.5	0.001109	58563.336764	41.0	0.000548	58676.819757	61.0	0.000798
58449.850482	21.0	0.000593	58566.164903	41.5	0.001345	58679.659708	61.5	0.002367

**Note.** Integer and half-integer cycle numbers refer to primary and secondary eclipses. For the ETV analysis, discussed in the main part of the paper, only primary eclipses were used. Primary eclipses marked with asterisks were omitted from the analysis as outliers.

### ORCID iDs

Pamela Rowden  <https://orcid.org/0000-0002-4829-7101>  
 Tamás Borkovits  <https://orcid.org/0000-0002-8806-496X>  
 Jon M. Jenkins  <https://orcid.org/0000-0002-4715-9460>  
 Keivan G. Stassun  <https://orcid.org/0000-0002-3481-9052>  
 Joseph D. Twicken  <https://orcid.org/0000-0002-6778-7552>  
 Elisabeth R. Newton  <https://orcid.org/0000-0003-4150-841X>  
 Carl Ziegler  <https://orcid.org/0000-0002-0619-7639>  
 Coel Hellier  <https://orcid.org/0000-0002-3439-1439>  
 Aylin García Soto  <https://orcid.org/0000-0001-9828-3229>  
 Elisabeth C. Matthews  <https://orcid.org/0000-0003-0593-1560>  
 Ulrich Kolb  <https://orcid.org/0000-0001-8670-8365>  
 George R. Ricker  <https://orcid.org/0000-0003-2058-6662>  
 Roland Vanderspek  <https://orcid.org/0000-0001-6763-6562>  
 David W. Latham  <https://orcid.org/0000-0001-9911-7388>  
 S. Seager  <https://orcid.org/0000-0002-6892-6948>  
 Joshua N. Winn  <https://orcid.org/0000-0002-4265-047X>  
 Luke G. Bouma  <https://orcid.org/0000-0002-0514-5538>  
 César Briceño  <https://orcid.org/0000-0001-7124-4094>  
 David Charbonneau  <https://orcid.org/0000-0002-9003-484X>

William Fong  <https://orcid.org/0000-0003-0241-2757>  
 Ana Glidden  <https://orcid.org/0000-0002-5322-2315>  
 Natalia M. Guerrero  <https://orcid.org/0000-0002-5169-9427>  
 Nicholas Law  <https://orcid.org/0000-0001-9380-6457>  
 Andrew W. Mann  <https://orcid.org/0000-0003-3654-1602>  
 Mark E. Rose  <https://orcid.org/0000-0003-4724-745X>  
 Joshua Schlieder  <https://orcid.org/0000-0001-5347-7062>  
 Peter Tenenbaum  <https://orcid.org/0000-0002-1949-4720>  
 Eric B. Ting  <https://orcid.org/0000-0002-8219-9505>

### References

- Aamio, A. N., Weinberger, A. J., Stassun, K. G., Mamajek, E. E., & James, D. J. 2008, *AJ*, **136**, 2483  
 Ahlers, J. P., Kruse, E., Colón, K. D., et al. 2020, *ApJ*, **888**, 63  
 Andrae, R., Fouesneau, M., Creevey, O., et al. 2018, *A&A*, **616**, A8  
 Bailer-Jones, C. A. L., Rybizki, J., Fouesneau, M., Mantelet, G., & Andrae, R. 2018, *AJ*, **156**, 58  
 Baraffe, I., Homeier, D., Allard, F., & Chabrier, G. 2015, *A&A*, **577**, A42  
 Bell, C. P. M., Mamajek, E. E., & Naylor, T. 2015, *MNRAS*, **454**, 593  
 Borkovits, T., Albrecht, S., Rappaport, S., et al. 2018, *MNRAS*, **478**, 5135  
 Borkovits, T., Hajdu, T., Sztakovics, J., et al. 2016, *MNRAS*, **455**, 4136  
 Borkovits, T., Rappaport, S., Hajdu, T., & Sztakovics, J. 2015, *MNRAS*, **448**, 946  
 Borkovits, T., Rappaport, S., Kaye, T., et al. 2019a, *MNRAS*, **483**, 1934

- Borkovits, T., Rappaport, S. A., Hajdu, T., et al. 2020, *MNRAS*, **493**, 5005
- Borkovits, T., Sperauskas, J., Tokovinin, A., et al. 2019b, *MNRAS*, **487**, 4631
- Brauer, R., Pantin, E., di Folco, E., et al. 2019, *A&A*, **628**, A88
- Breiter, S., & Vokrouhlický, D. 2018, *MNRAS*, **475**, 5215
- Bressan, A., Marigo, P., Girardi, L., et al. 2012, *MNRAS*, **427**, 127
- Buckley, D. A. H., Swart, G. P., & Meiring, J. G. 2006, *Proc. SPIE*, **6267**, 62670Z
- Chen, Z., Nürnberger, D. E. A., Chini, R., Jiang, Z., & Fang, M. 2015, *A&A*, **578**, A82
- Crause, L. A., Sharples, R. M., Bramall, D. G., et al. 2014, *Proc. SPIE*, **9147**, 91476T
- Davis, P. J., Kolb, U., & Willems, B. 2010, *MNRAS*, **403**, 179
- Duchêne, G., & Kraus, A. 2013, *ARA&A*, **51**, 269
- Farmer, R., Kolb, U., & Norton, A. J. 2013, *MNRAS*, **433**, 1133
- Fausnaugh, M. M., Valley, P. J., Kochanek, C. S., et al. 2019, arXiv:1904.02171
- Ford, E. B. 2005, *AJ*, **129**, 1706
- Gaia Collaboration, Brown, A. G. A., Vallenari, A., et al. 2018, *A&A*, **616**, A1
- Gaia Collaboration, Prusti, T., de Bruijne, J. H. J., et al. 2016, *A&A*, **595**, A1
- González, J. F., Hubrig, S., Nesvacil, N., & North, P. 2006, *A&A*, **449**, 327
- González, J. F., Hubrig, S., Nesvacil, N., & North, P. 2008a, in *Multiple Stars Across the H-R Diagram*, ed. S. Hubrig, M. Petr-Gotzens, & A. Tokovinin (Berlin: Springer), 259
- González, J. F., Nesvacil, N., & Hubrig, S. 2008b, in *Precision Spectroscopy in Astrophysics*, ed. N. C. Santos et al. (Garching: ESO), 291
- Guilloteau, S., Dutrey, A., & Simon, M. 1999, *A&A*, **348**, 570
- Güver, T., & Özel, F. 2009, *MNRAS*, **400**, 2050
- Helminiak, K. G., Ukita, N., Kambe, E., et al. 2017, *A&A*, **602**, A30
- Hippke, M., David, T. J., Mulders, G. D., & Heller, R. 2019, *AJ*, **158**, 143
- Holoien, T. W. S., Valley, P. J., Auchtell, K., et al. 2019, *ApJ*, **883**, 111
- Huber, D., Chaplin, W. J., Chontos, A., et al. 2019, *AJ*, **157**, 245
- Janson, M., Brandner, W., Lenzen, R., et al. 2007, *A&A*, **462**, 615
- Jayawardhana, R., Luhman, K. L., D'Alessio, P., & Stauffer, J. R. 2002, *ApJL*, **571**, L51
- Jenkins, J. M., Twicken, J. D., McCauliff, S., et al. 2016, *Proc. SPIE*, **9913**, 99133E
- Jenkins, J. M. 2019, AAS Meeting, **233**, 423.02
- Kniazev, A. Y., Gvaramadze, V. V., & Berdnikov, L. N. 2016, *MNRAS*, **459**, 3068
- Kniazev, A. Y., Gvaramadze, V. V., & Berdnikov, L. N. 2017, in *ASP Conf. Ser. 510, Stars: From Collapse to Collapse*, ed. Y. Balega et al. (San Francisco, CA: ASP), 480
- Koerner, D. W., Jensen, E. L. N., Cruz, K. L., Guild, T. B., & Gultekin, K. 2000, *ApJL*, **533**, L37
- Köhler, R. 2011, *A&A*, **530**, A126
- Kraus, A. L., Shkolnik, E. L., Allers, K. N., & Liu, M. C. 2014, *AJ*, **147**, 146
- Kurucz, R. L. 1993, *SYNTHES Spectrum Synthesis Programs and Line Data*, Kurucz CD-ROM (Cambridge, MA: Smithsonian Astrophysical Observatory)
- Lallement, R., Babusiaux, C., Vergely, J. L., et al. 2019, *yCat*, **J/A+A/625/** A135, 0
- Lee, C. U., Kim, S. L., Lee, J. W., et al. 2008, *MNRAS*, **389**, 1630
- Li, J., Tenenbaum, P., Twicken, J. D., et al. 2019, *PASP*, **131**, 024506
- Marks, M., & Kroupa, P. 2012, *A&A*, **543**, A8
- Mentuch, E., Brandeker, A., van Kerkwijk, M. H., Jayawardhana, R., & Hauschildt, P. H. 2008, *ApJ*, **689**, 1127
- Morris, R. L., Twicken, J. D., Smith, J. C., et al. 2017, *Kepler Data Processing Handbook: Photometric Analysis*, Kepler Science Document **KSCI-19081-002**
- Paxton, B., Bildsten, L., Dotter, A., et al. 2011, *ApJS*, **192**, 3
- Paxton, B., Cantiello, M., Arras, P., et al. 2013, *ApJS*, **208**, 4
- Paxton, B., Marchant, P., Schwab, J., et al. 2015, *ApJS*, **220**, 15
- Pollacco, D. L., Skillen, I., Collier Cameron, A., et al. 2006, *PASP*, **118**, 1407
- Pribulla, T., Baluďanský, D., Dubovský, P., et al. 2008, *MNRAS*, **390**, 798
- Pribulla, T., Puha, E., Borkovits, T., et al. 2020, *MNRAS*, **494**, 178
- Prša, A., & Zwitter, T. 2005, *ApJ*, **628**, 426
- Raghavan, D., McAlister, H. A., Henry, T. J., et al. 2010, *ApJS*, **190**, 1
- Rappaport, S., Vanderburg, A., Borkovits, T., et al. 2017, *MNRAS*, **467**, 2160
- Ribas, Á, Macías, E., Espaillat, C. C., & Duchêne, G. 2018, *ApJ*, **865**, 77
- Ricker, G. R., Vanderspek, R. K., Latham, D. W., & Winn, J. N. 2014, AAS Meeting, **224**, 113.02
- Riedel, A. R., Blunt, S. C., Lambrides, E. L., et al. 2017, *AJ*, **153**, 95
- Riello, M., de Angeli, F., Evans, D. W., et al. 2018, *A&A*, **616**, A3
- Schlafly, E. F., & Finkbeiner, D. P. 2011, *ApJ*, **737**, 103
- Schlegel, D. J., Finkbeiner, D. P., & Davis, M. 1998, *ApJ*, **500**, 525
- Schofield, M., Chaplin, W. J., Huber, D., et al. 2019, *ApJS*, **241**, 12
- Schönrich, R., McMillan, P., & Eyer, L. 2019, *MNRAS*, **487**, 3568
- Seok, J. Y., & Li, A. 2015, *ApJ*, **809**, 22
- Shkolnik, E. L., Allers, K. N., Kraus, A. L., Liu, M. C., & Flagg, L. 2017, *AJ*, **154**, 69
- Soderblom, D. R., King, J. R., Siess, L., et al. 1998, *ApJ*, **498**, 385
- Soderhjelm, S. 1975, *A&A*, **42**, 229
- Stassun, K. G., & Torres, G. 2016, *AJ*, **152**, 180
- Stassun, K. G., & Torres, G. 2018, *ApJ*, **862**, 61
- Sterzik, M. F., Melo, C. H. F., Tokovinin, A. A., & van der Bliik, N. 2005, *A&A*, **434**, 671
- Tokovinin, A. 2018, *PASP*, **130**, 035002
- Tokovinin, A., Corbett, H., Fors, O., et al. 2018, *AJ*, **156**, 120
- Tokovinin, A., Latham, D. W., & Mason, B. D. 2015, *AJ*, **149**, 195
- Tokovinin, A. A. 1999, *AstL*, **25**, 669
- Torres, G. 2004, *AJ*, **127**, 1187
- Torres, G., Ruíz-Rodríguez, D., Badenas, M., et al. 2013, *ApJ*, **773**, 40
- Tremaine, S. 2020, *MNRAS*, **493**, 5583
- Twicken, J. D., Catanzarite, J. H., Clarke, B. D., et al. 2018, *PASP*, **130**, 064502
- Twicken, J. D., Clarke, B. D., Bryson, S. T., et al. 2010, *Proc. SPIE*, **7740**, 774023
- Udalski, A., Szymański, M. K., & Szymański, G. 2015, *AcA*, **65**, 1
- Willems, B., & Kolb, U. 2002, *MNRAS*, **337**, 1004
- Willems, B., & Kolb, U. 2004, *A&A*, **419**, 1057
- Willems, B., Kolb, U., & Justham, S. 2006, *MNRAS*, **367**, 1103
- Willingale, R., Starling, R. L. C., Beardmore, A. P., Tanvir, N. R., & O'Brien, P. T. 2013, *MNRAS*, **431**, 394
- Wolter, U., Czesla, S., Fuhrmeister, B., et al. 2014, *A&A*, **570**, A95
- Zahn, J. P., & Bouchet, L. 1989, *A&A*, **223**, 112
- Zasche, P., & Uhlař, R. 2016, *A&A*, **588**, A121
- Zasche, P., Vokrouhlický, D., Wolf, M., et al. 2019, *A&A*, **630**, A128
- Zhan, Z., Günther, M. N., Rappaport, S., et al. 2019, *ApJ*, **876**, 127
- Ziegler, C., Tokovinin, A., Briceño, C., et al. 2020, *AJ*, **159**, 19